~~Mountain-wave induced~~ Mountain-wave-induced polar stratospheric clouds and their representation in the global chemistry model ICON-ART

Michael Weimer[1,2,*], Jennifer Buchmüller[2,†], Lars Hoffmann[3], Ole Kirner[1], Beiping Luo[4], Roland Ruhnke[2], Michael Steiner[5], Ines Tritscher[6], and Peter Braesicke[2]

[1]Steinbuch Centre for Computing, Karlsruhe Institute of Technology (KIT), Eggenstein-Leopoldshafen, Germany
[2]Institute of Meteorology and Climate Research, Karlsruhe Institute of Technology (KIT), Eggenstein-Leopoldshafen, Germany
[3]Jülich Supercomputing Centre, Forschungszentrum Jülich, Jülich, Germany
[4]Institute for Atmospheric and Climate Science, ETH Zurich, Switzerland
[5]Laboratory for Air Pollution / Environmental Technology, EMPA, Switzerland
[6]Institute of Energy and Climate Research: Stratosphere (IEK-7), Forschungszentrum Jülich, Jülich, Germany
[*]now at: Department of Earth, Atmospheric and Planetary Sciences, Massachusetts Institute of Technology, Cambridge, MA, USA
[†]now at: Steinbuch Centre for Computing, Karlsruhe Institute of Technology (KIT), Eggenstein-Leopoldshafen, Germany
Correspondence: Michael Weimer (michael.weimer@kit.edu)

Abstract. Polar stratospheric clouds (PSCs) are a driver for ozone depletion in the lower polar stratosphere. They provide surfaces for heterogeneous reactions activating chlorine and bromine reservoir species during the polar night. The large-scale effects of PSCs are represented by means of parametrisations in current global chemistry-climate models, but one process is still a challenge: the representation of PSCs formed locally in conjunction with unresolved mountain waves. In this study, we ~~present simulations~~ investigate direct simulations of PSCs formed by mountain waves with the ICOsahedral Nonhydrostatic modelling framework (ICON) with its extension for Aerosols and Reactive Trace gases (ART) ~~that include~~ including local grid refinements (nesting) with two-way interaction. Here, the nesting is set up around the Antarctic Peninsula which is a well-known hot spot for the generation of mountain waves in the southern hemisphere. We compare our model results with satellite measurements of PSCs from the Cloud-Aerosol LIdar with Orthogonal Polarisation (CALIOP) and gravity wave observations of the Atmospheric InfraRed Sounder (AIRS). ~~We study~~ For a mountain wave event ~~that took place~~ from 19 to 29 July 2008 ~~and~~ we find similar structures of PSCs as well as a fairly realistic development of the mountain wave between the satellite data and the ICON-ART simulations in the Antarctic Peninsula nest. We compare a global simulation without nesting with the nested configuration to show the ~~benefit~~benefits of adding the nesting. Although the mountain waves cannot be resolved ~~adequately~~ explicitly in the used global resolution (about $160\,\mathrm{km}$), their effect from the nested regions (about 80 and $40\,\mathrm{km}$) on the global domain is represented. Thus, we show in this study that ~~by using the two-way nesting technique the~~ the ICON-ART model has the potential to bridge the gap between directly resolved ~~mountain-wave induced~~ mountain-wave-induced PSCs and their representation and effect on chemistry in coarse global resolutions~~can be bridged by the ICON-ART model~~.

1 Introduction

Polar stratospheric clouds (PSCs) play a key role in explaining the rapid ozone loss in the polar stratosphere during local spring (e.g., Solomon et al., 1986; Solomon, 1999; Braesicke et al., 2018). Three different types of PSCs or mixtures thereof can be found in the lower stratosphere: solid nitric acid trihydrate particles (NAT), liquid supercooled ternary solution droplets (STS) and ice particles (e.g., Peter and Grooß, 2012; Tritscher et al., 2021, and references therein). Heterogeneous reactions on the surface of PSCs lead to activation of chlorine and bromine species during the polar night, thus enhancing the catalytic ozone depletion cycles as soon as the sun rises (e.g., Solomon, 1999). In addition, PSCs can irreversibly remove nitrogen-containing species by sedimentation, ~~today~~ a process known as denitrification, thus extending the period of low ozone concentrations during polar spring (e.g., Waibel et al., 1999).

~~One of the processes under investigation is PSCs formed in conjunction with mountain waves. It is known that mountain-wave induced PSCs have a significant influence on the ozone depletion over Antarctica and Arctic (e.g., McDonald et al., 2009; Alexander et al.,~~ ~~. However, the simulation of mountain-wave induced PSCs with atmospheric chemistry models (ACMs) is still a challenge (e.g., Orr et al., 2015). With horizontal resolutions in the order of a few hundreds of kilometres, ACMs are not able to resolve the orography adequately to directly simulate mountain waves (Morgenstern et al., 2010). Thus, mountain waves and mountain-wave induced PSCs either have to be parametrised (Orr et al., 2015; Zhu et al., 2017; Orr et al., 2020) or have to be calculated as post-processing via Lagrangian models (e.g., Mann et al., 2005) or higher resolved mesoscale models (e.g., Fueglistaler et al., 2003; Eckerm , which have to be limited to a specific region on Earth as discussed e.g. in Weimer et al. (2016). A method to bridge this gap for interactive calculations is missing so far~~ PSCs may form below specific threshold temperatures (e.g., Hanson and Mauersberger, 1988; Marti , indicating that temperature is a crucial parameter for PSC formation.

~~Three types of PSCs are known to exist: (1) solid nitric acid trihydrate (NAT) particles, mostly responsible for denitrification (e.g., Fahey et al., 2001), (2) liquid supercooled ternary solution (STS) droplets which grow from the background sulfate aerosol (Junge et al., 1961; Wilka et al., 2018) by taking up nitric acid (HNO₃) and on which the major fraction of chlorine and bromine activation takes place (e.g., Peter, 1997; Kirner et al., 2015) and (3) ice clouds forming at the lowest temperatures and leading to dehydration of the lower stratosphere (e.g., Kelly et al., 1989; Khaykin et al., 2013).~~

~~Various climatologies of PSCs based on satellite measurements were published in the last years (Spang et al., 2018; Höpfner et al., 2018; . The application of machine learning for the detection of PSCs from satellite measurements has been discussed recently (Sedona et al., 2020).~~

~~Nucleation processes especially of NAT and ice PSCs are still under debate (e.g., Voigt et al., 2018). The question if equilibrium or non-equilibrium processes are needed to describe the growth of STS particles is an issue of research (Zhu et al., 2015). In addition, it is also known that mountain waves can induce PSCs which influence the ozone chemistry (e.g., Hoffmann et al., 2017) .~~

Mountain waves (orographic gravity waves) are stationary waves in the lee of a mountain which can develop in a stably stratified atmosphere (e.g., Fritts and Alexander, 2003) ~~. They~~ when the large scale flow is perpendicular to the mountain range. Mountain waves can propagate upwards into the stratosphere and higher (Wright et al., 2017) and may perturb the synoptic tem-

perature field with ~~a local amplitude in the order~~ local amplitudes of up to ~~±15 K (Meilinger et al., 1995; Carslaw et al., 1998a; Eckermann~~ ~~.~~ ±15 K or even more (Carslaw et al., 1998b; Eckermann et al., 2009; Dörnbrack et al., 2020). In the polar regions, mountain waves are of particular interest for the formation of PSCs because mountain-wave-induced temperature fluctuations can lead

55 to localised cooling that triggers PSC formation even if synoptic-scale temperatures are above the PSC formation temperatures (Carslaw et al., 1998b).

~~Apart from heterogenenous nucleation of NAT on meteoric dust (e.g., Hoyle et al., 2013; Tritscher et al., 2019), denitrification in the Arctic region is closely connected to mountain wave activity because large NAT particles can be formed in the low temperatures associated with mountain waves~~ Mountain-wave-induced PSCs have a significant influence on the ozone depletion

60 over both Antarctica and the Arctic (e.g., Höpfner et al., 2006a; McDonald et al., 2009; Alexander et al., 2011; Hoffmann et al., 2017; Lang ~~.~~ Various regions have been identified from observations and models as being hot spots for mountain-wave-induced PSCs, such as Greenland and Scandinavia in the northern hemisphere ~~(e.g., Tabazadeh et al., 2000). On the other hand, mountain-wave induced PSCs are also important for the southern hemisphere. Antarctic mountain-wave induced NAT PSCs were detected by Höpfner et al. (2006a) for the first time. McDonald et al. (2009) stated~~ and the Southern Andes, the Antarctic Peninsula or the

65 Transantarctic Mountains in the southern hemisphere (Dörnbrack et al., 2002; Plougonven et al., 2008; Eckermann et al., 2009; Noel et al., ~~.~~ McDonald et al. (2009) estimated that up to 40 % of ~~PSC formation comes from~~ Antarctic PSC formation are associated with mountain waves in the early Antarctic winter when ~~temperature is close to that of NAT formation . Alexander et al. (2011)~~ temperatures are close to the NAT formation threshold. Alexander et al. (2013) concluded that about ~~30 % of all southern hemispheric PSCs can be~~ 5 % of Antarctic and 12 % of Arctic PSCs are related to mountain ~~waves.~~ wave activity.

70 Mountain waves are mesoscale features of the atmospheric circulation, which poses a challenge for simulating them explicitly with global general circulation models because these models have limited spatial resolution. The horizontal wavelengths of mountain waves most relevant for the middle atmosphere are in the range of tens to hundreds of kilometres (e.g., Fritts and Alexander, 2003; ~~.~~ Several studies suggest that in a discrete numerical model eight grid points are needed to represent gravity waves and their dynamics adequately (Geller et al., 2013; Preusse et al., 2014; Kang et al., 2017). However, current global chemistry climate

75 models (CCMs) with horizontal resolutions in the order of a few hundreds of kilometres are not able to resolve the full range of mountain waves adequately (Lamarque et al., 2013; Orr et al., 2015; Morgenstern et al., 2017). Mesoscale models with resolutions as high as 7 km have been developed in the past to calculate the local effect of mountain-wave-induced PSCs (e.g., Fueglistaler et al., 2003; Eckermann et al., 2006; Plougonven et al., 2008; Noel and Pitts, 2012) but they need input of a previous simulation of a global model or a reanalysis to provide the boundary conditions (e.g., Weimer et al., 2016). Thus,

80 mountain waves and mountain-wave-induced PSCs either have to be parametrised (Orr et al., 2015; Zhu et al., 2017; Orr et al., 2020) or have to be calculated in a post-processing step via Lagrangian models (e.g., Mann et al., 2005) or via mesoscale models. An approach for interactive two-way coupling between the high-resolution simulations and the global models, in particular CCMs, is missing so far.

In this study, ~~mountain-wave induced~~ mountain-wave-induced PSCs are simulated seamlessly with the ICOsahedral Nonhy-

85 drostatic modelling framework (ICON, Zängl et al., 2015) and its extension for Aerosols and Reactive Trace gases (ART, Rieger et al., 2015; Weimer et al., 2017; Schröter et al., 2018). ICON-ART provides the possibility of local grid refinement (nesting)

with two-way interaction ~~so that a coarse global resolution can be complemented by~~ (see Reinert et al., 2019, for details). Thus, a low resolution drives a region with ~~a refined grid(Reinert et al., 2019), such as the Antarctic Peninsula which is one of the hot spots for the generation of southern hemispheric mountain waves (Bacmeister, 1993; Bacmeister et al., 1994; McDonald et al., 2009; Alexa~~

90 ~~. Therefore, mountain-wave induced PSCs can be directly simulated with~~ refined grid, similar to mesoscale models. But additionally, the refined grid also feeds back to the low resolution which is a novel approach in atmospheric chemistry modelling.

We perform a comprehensive case study for a well-observed mountain wave event at the Antarctic Peninsula in July 2008 (Noel and Pitts, 2012). We start at a global resolution of about 160 km which is comparable to other global CCMs. We then

95 apply the two-way nesting at the Antarctic Peninsula with a resolution of 40 km in the grid refinement. This resolution still misses directly resolving gravity waves with horizontal wavelengths lower than about 300 km (cf., Geller et al., 2013), but we chose this configuration (1) for a balance between accuracy and computational expense and (2) to show how CCMs could already benefit from modest higher resolutions. We show how the higher resolution in the refinement impacts the gravity wave dynamics, PSCs and finally the ozone chemistry in the global model. Thus, this study is a first step to close the gap between

100 direct simulations of mountain-wave-induced PSC formation and their treatment in coarse global resolutions.

We selected the Antarctic Peninsula for this study with the ICON-ART ~~in the refined grid (nest) and their effect can be treated at the global resolution in the same simulation where they cannot be resolved without the nest.~~model because it is a well-known hot spot of mountain-wave-induced PSCs (Bacmeister, 1993; Bacmeister et al., 1994; McDonald et al., 2009; Alexander et al., 2011; Hoff. Given the strong incident flow at low levels and the Antarctic Peninsula protunding a distance of 1300 km with peak heights

105 of up to 2800 m posing a substantial barrier to this flow, mountain waves with large amplitudes, and large horizontal (> 300 km) and vertical wavelengths (> 10 km) are typically excited (Alexander and Teitelbaum, 2007; Plougonven et al., 2008; Hoffmann et al., 2013. Thus, our ICON-ART model configuration is expected to be able to capture such waves.

~~The~~ Despite the Antarctic Peninsula being in a remote location, it is frequently covered by gravity wave and PSC satellite observations that allows to evaluate the ICON-ART simulations (e.g., Hoffmann et al., 2016; Spang et al., 2018; Höpfner et al., 2018; Pitts

110 . Here, we specifically use Atmospheric InfraRed Sounder (AIRS, Aumann et al., 2003; Chahine et al., 2006) and Cloud-Aerosol LIdar with Orthogonal Polarisation (CALIOP, Pitts et al., 2009; Höpfner et al., 2009; Pitts et al., 2018) data to evaluate our simulations. AIRS is a cross-track scanning nadir instrument that is able to detect stratospheric temperature fluctuations with high horizontal resolution (up to 14 km at nadir). Therefore, it is particularly suited to detect the horizontal structures of mountain waves in the lower and mid stratosphere (e.g., Hoffmann et al., 2013, 2017). CALIOP, a nadir lidar instrument with

115 high resolution in both horizontal (5 km) and vertical (180 m in the lower stratosphere) direction, can detect and discriminate the different types of PSCs (Pitts et al., 2018). Therefore, CALIOP is able to identify PSCs formed in mountain waves and can be used for the evaluation of PSC schemes in models. Sampling the model results on the measurement grid of the satellite instruments and converting the data from model quantities to measured quantities (e.g., by means of radiative transfer calculations) is a precise way to evaluate the ICON-ART simulations with AIRS and CALIOP observations (Mishchenko et al., 1996; Grims

120 .

This study is organised as follows: Section 2 briefly describes the ICON-ART model ~~is described in Sect. 2,~~ and its PSC scheme. In Sect. 3, the simulation setup is pointed out that is used to examine the mountain wave event at the Antarctic Peninsula. This is followed by a description of the ~~simulation in Sect. 3 and the satellite data used for comparison with ICON-ART~~ AIRS and CALIOP instruments in Sect. 4. The model results are compared with CALIOP and AIRS measurements

125 and ~~mountain-wave induced PSCs are investigated for a typical mountain wave event~~ the impact of the two-way nesting on the chemstry is investigated in Sect. 5. Finally, conclusions and outlook follow in Sect. 6.

2 The ICON-ART model

The ICON model is the operational model for numerical weather prediction at the German Weather Service (DWD, Zängl et al., 2015). In addition, it can be applied to large eddy simulations (Dipankar et al., 2015) and fully coupled with an ocean

130 and a land surface model for climate integrations with the climate physics configuration (Giorgetta et al., 2018). The ART extension has been developed to incorporate aerosols and the atmospheric chemistry into ICON. It can be coupled to ICON in configurations for numerical weather prediction (Rieger et al., 2015) and allows flexible configurations for weather and climate integrations (Schröter et al., 2018).

~~In this study, the~~ The PSC scheme in ICON-ART calculates ice PSCs based on the microphysics of the operational configuration

135 at DWD (Doms et al., 2011). For stratospheric temperatures, the microphysics assumes an ice number concentration of $0.25\,\mathrm{cm}^{-3}$. Liquid (sulfate and STS) particles are formed by the module of Carslaw et al. (1995), with some adaption of the used size distributions. NAT particles are formed by a non-equilibrium approach based on Carslaw et al. (2002) and van den Broek et al. (2004). The NAT size distribution can be flexibly selected by the model user via XML files (see Schröter et al., 2018). A maximum NAT number concentration of $2.3 \times 10^{-4}\mathrm{cm}^{-3}$ is assumed (van den Broek et al., 2004). The PSC particles are treated separately

140 and externally mixed in each grid box. A detailed description of the PSC scheme can be found in Appendix A.

While STS particles are calculated diagnostically, NAT particles are separate tracers for each size bin. Both NAT and ice include prognostic equations that allow the advection of these particles into regions with temperatures too large for PSC formation, which has been observed in mountain waves (Eckermann et al., 2009). The other parts of the scheme are designed similar to global models like ECHAM/MESSy Atmospheric Chemistry model (EMAC, Jöckel et al., 2010; Kirner et al., 2011)

145 which have been shown to reflect the main properties of PSCs on a global scale. This study focuses on the benefit of increasing the resolution and showing the impact of the two-way nesting.

The chemistry in ICON-ART is based on the Module Efficiently Calculating the Chemistry of the Atmosphere (MECCA, Sander et al., 2011a) which uses the Kinetic PreProcessor (KPP) to generate Fortran files for solving the specified chemical mechanism (Sandu and Sander, 2006). Photolysis rates are calculated with the CloudJ module (Prather, 2015; Weimer et al.,

150 2017). ~~In this study, a~~ A system of 142 chemical reactions including 38 photolytic reactions and 11 heterogeneous reactions on the surface of PSCs is used~~which~~. It covers the chemical families O_x, HO_x, NO_x, ClO_x, BrO_x, a basic hydrocarbon chemistry and the oxidation of SO_2. The reaction system is similar to other studies (e.g., Stone et al., 2019; Zambri et al., 2019; Nakajima
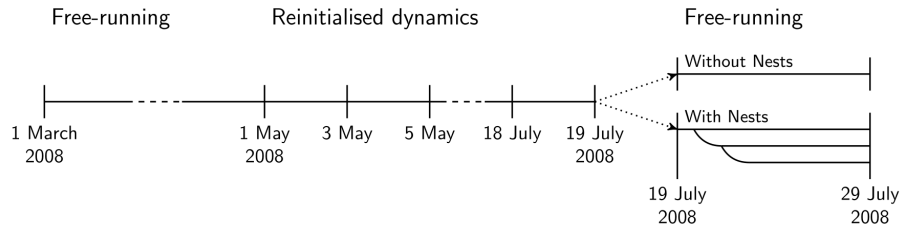
Figure 1. Simulation setup in this study: A free-running simulation from 01 March 2008 until 30 April 2008 is followed by a period until 18 July 2008 where the meteorology is reinitialised every second day. During the mountain wave event until 29 July 2008, two simulations are performed: one global simulation without nests (with 160 km resolution) and one simulation with the nests (with 160, 80 and 40 km resolution) as visualised in Fig. 2 including two-way nesting.

et al., 2020) and can be found in ~~Appendix ??~~the supplement. Trace gas emissions at the Earth's surface are included by a module described in Weimer et al. (2017).

The model equations of ICON-ART are discretised horizontally on an icosahedral-triangular C grid (e.g., Staniforth and Thuburn, 2012; Zängl et al., 2015). The global resolution can be refined by root divisions and bisections of the original icosahedron, resulting in the horizontal resolution description RnBk, as defined by e.g. Zängl et al. (2015). Vertical discretisation is performed on generalised smooth-level coordinates (Leuenberger et al., 2010).

For the purpose of detailed simulations around a specific region, the grid can be refined for the area of interest by further bisections. Here, the parent domain provides boundary conditions for the nested domain. The simulated values in the nested domain are interpolated to the parent grid with a relaxation-based method (Reinert et al., 2019). Thus, the ~~two-way nesting enables the model to simulate e.g. mountain waves directly at hot spots and also to impact the variables at a global resolution that is too coarse to represent these processes.~~ global domain is nudged towards the values in the nests, which will be further investigated in Sect. 5.

2.1 ~~The PSC scheme~~

3 Simulation with nests around the Antarctic Peninsula

In ~~ICON-ART, the three types of PSCs (ice, NAT and STS) are treated separately. Sensitivity simulations showed that the ICON microphysics for ice clouds, operationally computed up to an altitude of , can be extended to the lower stratosphere up to (Weimer, 2019). The hydrometeor microphysics in ICON include several nucleation processes interacting with the other hydrometeors as well as sedimentation of the ice particles (Doms et al., 2011). Thus, both nucleation of ice PSCs and dehydration of the lower stratosphere can be captured by the ICON microphysics. A similar approach is used in the Whole Atmosphere Community Climate Model (WACCM, Zhu et al., 2015). Ice particle radius (r_{ice} in) and particle number~~

concentration (N_{ice} in) correspond to the assumed size distributions in the microphysics (Doms et al., 2011):

$$N_{ice}(T) = \min\left(5\exp\left[0.304\left(273.15 - T\right)\right], 250 \times 10^3\right)$$

$$r_{ice} = \tfrac{1}{2}$$

$]\frac{\rho\, q_{ice}}{130\, N_{ice}}$ where ρ is the air density in , q_{ice} is the mass mixing ratio in of water in ice. 2008, a mountain-wave event took place between 19 and 29 July around the Antarctic Peninsula (Noel and Pitts, 2012) which is further investigated in this study. A three-step simulation is conducted, see Fig. 1.

Two parametrisations for the microphysics of NAT particles are integrated in ICON-ART. The thermodynamic NAT parametrisation is diagnostic and therefore computes the number of moles of NAT particles in thermodynamic equilibrium, calculates its sedimentation and evaporates the particles again within the same model time step. The volume mixing ratio of HNO_3 condensed in NAT ($X_{HNO_3(NAT)}$ in) is calculated on the basis of the difference between vapour pressure of HNO_3 (p_{HNO_3} in) and the saturation vapour pressure over NAT ($p_{sat,NAT}$ in):

$$X_{HNO_3(NAT)} = \frac{p_{HNO_3} - p_{sat,NAT}}{p}$$

The saturation vapour pressure over NAT is calculated according to Hanson and Mauersberger (1988) and p is the air pressure (in). Particle number concentration (N_{NAT}) and radius (r_{NAT}) in the thermodynamic NAT parametrisation are calculated using a threshold in the number concentration of $N_{NAT,max} = 2.3 \times 10^{-4}\,\mathrm{cm}^{-3}$ which originates from observations (Fahey et al., 2001). Below this threshold, the radius of the NAT particles is set to . Above this threshold, the particle number concentration is set to $N_{NAT,max}$ and the radius of the particles is increased accordingly. This method has already been used in a similar way for solid particles by Kirner et al. (2011). In the first step, the simulation starts on 01 March 2008 with a global resolution of R2B04 (Δx of about $160\,\mathrm{km}$) as a free-running simulation until 01 May 2008. The first of March is chosen because almost no PSCs are formed at this time either in the northern or in the southern hemisphere (Tully et al., 2011). This period is used as a spin-up period for the chemistry until the southern hemispheric polar vortex intensifies (Schoeberl and Newman, 2003) and PSCs formed in 2008 (Tully et al., 2011).

The kinetic NAT parametrisation is a non-equilibrium approach based on prognostic equations for the particle mass (see e.g., Seinfeld and . Carslaw et al. (2002) applied this approach to NAT particles in a Lagrangian model and van den Broek et al. (2004) extended it to Eulerian models. Size distribution of NAT particles used in this study. Based on van den Broek et al. (2004).

In the Lagrangian description by Carslaw et al. (2002), the change in NAT particle radius ($r_{NAT,b}$) is calculated prognostically by a diffusive growth

where G_b (in) is a growth factor which depends on the diffusion coefficient of HNO_3 in air (D_{HNO_3}, second step, the meteorological variables are reinitialised every second day by the reanalysis product of ECMWF, ERA-Interim (Dee et al., 2011)

205 , in), the air temperature (T, in) and the saturation difference of the vapour pressure (in):

with

210

In these equations, $\overline{v}_{\mathrm{HNO_3}}$ is the mean thermal velocity of air molecules (in), R^* stands for the universal constant of an ideal gas in , ρ_{NAT} is the crystal density of NAT ($1.626 \times 10^6\,\mathrm{g\,m^{-3}}$, Drdla et al., 1993; van den Broek et al., 2004) and M_{NAT} is

215 the NAT molar mass of . In one of the Eulerian formulations by van den Broek et al. (2004), this radius change is applied to particles in size bins, but directly converted into a change in the particle number concentration ("FixedRad" approach). This approach is used in this study with a size distribution based on van den Broek et al. (2004) as shown in Fig.3. That is why we added a b subscript to all variables in Eqs. , and that depend on the size bin b.

The size distribution of NAT particles can be flexibly specified by the user to investigate its impact on denitrification without

220 any change in the Fortran code but rather changing the respective XML control file (cf. Schröter et al., 2018). Each size bin is defined by radius limits and a maximum particle number concentration, which are kept constant during the simulation . If the calculated particle number concentration in a bin exceeds the maximum, the excess mass is transferred to the next larger size bin. The sum of the maximum particle number concentrations of the bins has to equal the observed value by Fahey et al. (2001) , which is . The size bins are transported as passive tracers in ICON-ART. period between 01 May and 18 July 2008, but the

225 chemical tracers are free-running. This ensures a comparable evolution of the polar vortex in the model with respect to the reanalysis. This method was already introduced e.g. in Schröter et al. (2018).

Since the calculation of $p_{\mathrm{sat,NAT}}$ by Hanson and Mauersberger (1988) has specific temperature limits, NAT particles are evaporated automatically at temperatures higher than . For temperatures below , we calculate $p_{\mathrm{HNO_3}}$ with a constant temperature of . These two NAT parametrisations are also implemented in the ECHAM/MESSy Atmospheric Chemistry model (EMAC, Jöckel et al., 20

230 .

Sedimentation of NAT particles, either formed by thermodynamic or kinetic NAT parametrisation, is calculated by a simple upwind method, using the Stokes velocity of assumed spherical particles (Stokes, 1851).

The microphysics of STS particles in the module are calculated by the scheme first published by Carslaw et al. (1995), with one exception: in the original code by Carslaw et al. (1995) the particle number concentration is set to the constant value of .

235 We improved this fixed value by applying the mean of all balloon-borne STS measurements by Hervig and Deshler (1998) in
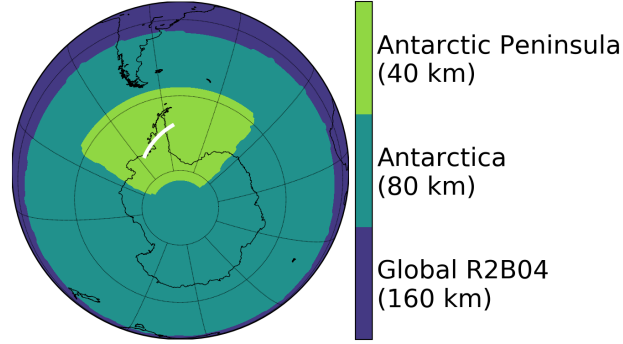
Figure 2. Visualisation of the nested domains used in the simulation with the nests: A global resolution of R2B04 ($\Delta x \approx 160\,\text{km}$) is used, with first circular refined grid around the Antarctic Continent (R2B05, $\Delta x \approx 80\,\text{km}$) and a second rectangular refinement around the Antarctic Peninsula (R2B06, $\Delta x \approx 40\,\text{km}$). The white line shows the location of the cross section analysed in Sect. 5.4.

Table 1. Overview of the simulation setup for the investigation of the mountain wave event in July 2008. Details see text.

Time period (in 2008)	Resolution	Output interval (h)	Remark
01 March – 30 April	R2B04	24	Spin-up for chemistry, free-running
01 May – 18 July	R2B04	24	Dynamics reinitialised every second day
19 July – 29 July	R2B04	1	Free-running
	see Fig. 2	see text	Including two-way nesting

~~order to derive the particle surface area concentration S_{STS} and the radius r_{STS} of STS particles from the internally calculated particle volume concentration V_{STS}:~~

$$\underline{S_{\text{STS}} \quad = 6.068\,(V_{\text{STS}})^{0.671}}$$

$$\underline{r_{\text{STS}} \qquad = \frac{3\,V_{\text{STS}}}{S_{\text{STS}}}}$$

240 ~~In these equations, V_{STS} has to be given in to get S_{STS} and r_{STS}~~ In the third step, we conducted two simulations covering the mountain wave event from 19 to 29 July 2008: one simulation without any nests and one simulation with two-way nesting around the Antarctic Continent (R2B05, Δx of about $80\,\text{km}$) and around the Antarctic Peninsula (R2B06, Δx of about $40\,\text{km}$), see Fig. 2 and Table 1. The chemistry, including PSCs, photolysis and transport of tracers, is calculated in ~~and , respectively. Sedimentation is neglected for STS particles since they are too small to result in relevant redistribution of the major constituents~~

245 ~~H_2O, HNO_3 and H_2SO_4 (Tabazadeh et al., 2000; Considine et al., 2000).~~

~~Since the PSCs in the current version of the model do not interact with each other like in a fully coupled PSC scheme (e.g., Zhu et al., 2015), there are essentially two approaches to calculate PSCs: either they are computed with the total (gaseous + liquid + solid) concentrations of and as input for all PSC types (e.g., Kirner et al., 2011) or the PSCs are calculated subsequently~~

~~with the gaseous fraction that remains after formation of the previously calculated PSC types (operator splitting). Both approaches have their advantages and disadvantages. We use the second approach because the maximum of and taken up by PSCs cannot exceed the gaseous concentrations in this case. First, ice PSCs are calculated, then NAT PSCs and finally STS PSCs.~~

~~Particle radius, particle number concentration and particle surface area concentration are used to calculate the heterogeneous reaction rate constants on the surface of PSCs. For NAT and ice, which can grow to relatively large sizes in the order of tens of , the following equation is used to calculate the heterogeneous reaction rate constant, assuming spherical particles (Drdla et al., 1993):~~

~~where $\gamma_{h,c}$ is the uptake coefficient (i.e. reaction probability) of heterogeneous reaction h and PSC type c, $\bar{v}_{i(h)}$ is the mean thermal velocity of~~ all domains. Since we are interested in ~~the gaseous reactant $i(h)$ (in), N_c is the PSC number concentration and $N_{j(h)}$ is the number concentration of the reactant $j(h)$ adsorbed on the particle (both in) . The Knudsen number Kn is calculated by $\lambda_{\mathrm{mfp}}/r_c$ with the mean free path λ_{mfp} of air molecules (in), calculated according to Kennard (1938). In case of the kinetic NAT parametrisation, Eq. is evaluated for each size bin separately and summed up subsequently.~~ interaction between the model domains, we decided to avoid every influence by other models during this part of the simulation and hence they are free-running. Output in this third step of the simulation is given (1) at the specific Antarctic Peninsula overpasses of AIRS for the Antarctic Peninsula nest and (2) hourly during the whole period of the mountain wave event.

~~STS particles are considerably smaller than ice and NAT particles (e.g., Considine et al., 2000) and hence Kn $\gg$ 1 so that the slip flow correction term in Eq. can be neglected, which yields:~~

~~The total reaction rate constant is the sum of the reaction rate constants on all three types of PSCs. The uptake coefficients in ICON-ART are used either from Carslaw et al. (1995) or Sander et al. (2011b). A summary of the γ values can be found in Table ?? of Appendix ??. They also compare well to other models (e.g., Solomon et al., 2015).~~

4 ~~Simulation with nests around the Antarctic Peninsula~~

~~Simulation setup in this study: A free-running simulation from 01 March 2008 until 30 April 2008 is followed by a period until 18 July 2008 where the meteorology is reinitialised every second day. During the mountain wave event until 29 July 2008, two~~

Table 2. Emission datasets used in this study.

Species	GEIA[a]	MACCity[b]	MEGAN-MACC[c]	GFED3[d]	EDGARv4.2[e]
CH_4	–	✓	✓	✓	–
CO	–	✓	✓	–	✓
CO_2	–	–	–	✓	✓
N_2O	–	–	–	✓	✓
SO_2	–	✓	–	✓	–
$CFCl_3$	✓	–	–	–	–

[a] Cunnold et al. (1994)

[b] van der Werf et al. (2006); Lamarque et al. (2010); Granier et al. (2011); Diehl et al. (2012)

[c] Sindelarova et al. (2014)

[d] van der Werf et al. (2010)

[e] Janssens-Maenhout et al. (2011, 2013)

280 ~~simulations are performed: one global simulation without nests (with resolution) and one simulation with the nests (with , and resolution) as visualised in Fig. 2 including two-way nesting.~~

~~In order to compare the results of the PSC scheme in ICON-ART with satellite measurements and to investigate the impact of the nesting technique on mountain-wave induced PSCs, a three-step simulation is conducted, see Fig. 1. The~~ On 01 March 2008, the meteorological variables are initialised with ~~the reanalysis product of the European Centre for Medium-Range Weather Forecasts (ECMWF)~~ ERA-Interim ~~(Dee et al., 2011) on 01 March 2008. The first of March is chosen because almost no PSCs~~
285 ~~are formed at this time either in the northern or in the southern hemisphere. In 2008, a mountain-wave event took place between 19 and 29 July around the Antarctic Peninsula (Noel and Pitts, 2012) which is further investigated in this study~~. The chemical tracers are initialised by an EMAC simulation which included tropospheric as well as stratospheric chemistry similar to Jöckel et al. (2016). Sea surface temperature and sea ice cover are based on monthly varying values of the climatology by Taylor et al. (2000), linearly interpolated to the simulation date. The advective model time step is set to $360\,s$. Vertically, the
290 same 90 levels are used as in the operational setup of DWD weather forecasts, covering the altitude range from the surface up to $75\,km$ (see e.g., Weimer et al., 2017, Fig. 1). In the lower stratosphere, the vertical grid spacing increases from $400\,m$ at an altitude of $12\,km$ up to about $1200\,m$ at $30\,km$.

~~The chemical trace gases (tracers) are initialised by an EMAC simulation which included tropospheric as well as stratospheric chemistry similar to Jöckel et al. (2016). NAT PSCs are simulated with the kinetic NAT parametrisation. The size distribution~~
295 ~~is shown in Fig. 3. We prescribe H₂SO₄ in the lower stratosphere (Thomason et al., 2008; SPARC, 2013).~~

The emission ~~data sets~~ datasets used in this study are summarised in Table 2. Emissions of CH_4, CO, CO_2, N_2O, SO_2 and $CFCl_3$ are considered. The GEIA dataset for chlorofluorocarbons (CFCs) provided by the Emissions of atmospheric Compounds and Compilation of Ancillary Data base (ECCAD) includes only the year 1986 and should eventually be adapted

Figure 3. Size distribution of NAT particles used in this study. Based on van den Broek et al. (2004).

by the online emission tool by Jähn et al. (2020) for the simulated year. ~~This is why other CFCs, apart from~~ Since the emission rates of CFCl$_3$ ~~, are neglected in the~~ have decreased by more than $40\,\%$ since 1986 (Montzka et al., 2018), we neglect the emissions of other CFCs for the less than 1-year simulation~~(see below) of this study which is therefore dominated by the initialisation of the chemical species. In the~~. In combination with the emission tool by Jähn et al. (2020) and in the context of the recently found source of CFCs (Montzka et al., 2018; Lickley et al., 2020), further CFCs should be considered in future simulations.

~~In the first step, the simulation starts with a global resolution of R2B04 (Δx of about) as a free-running simulation until 01 May 2008. This period is used as a spin-up period for the chemistry until the southern hemispheric polar vortex begins to form. The resolution of is comparable to current chemistry climate models (e.g., Morgenstern et al., 2010; Kirner et al., 2015; Zhu et al., 2015; ?). Thus, this simulation shows how mountain-wave induced PSCs can be treated in a resolution that is similar to other chemistry climate models.~~

~~In the second step, it is of importance that the dynamics of the atmosphere and especially the polar vortex are represented realistically in the model, especially for the evaluation with measurement data. This is why the meteorological variables are reinitialised every second day by ERA-Interim in the period between 01 May and 18 July 2008, but the chemical tracers are free-running. This method was already introduced e.g. in Schröter et al. (2018).~~

~~Simulation setup: The first two months from 01 March to 30 April 2008 are a spin-up period for the chemical tracers. Then, the dynamical variables are reinitialised every second day until 18 July 2008. During the mountain wave event, two simulations are performed: one simulation without any nests and one simulation with the nests. Output in the simulation with nests is hourly~~

and at the specific Antarctic Peninsula overpasses of AIRS analysed in Sect. 5.3. Time period Resolution Output interval (h) Remark 01 March – 30 April R2B04 24 Spin-up for chemistry, free-running 01 May – 18 July R2B04 24 Dynamics reinitialised every second day R2B04 1 Free-runningsee Fig. 2 see main text Including two-way nesting

320 In the third step, to avoid the determination of the simulations by lower resolution models and models with hydrostatic dynamical core, two different free-running simulations are conducted during the mountain wave event from 19 to 29 July 2008: one simulation without any nests and one simulation with nests around the Antarctic Continent (R2B05, Δx of about) and around the Antarctic Peninsula (R2B06, Δx of about), see Fig. 2 and Table 1. Output in this part of the simulation is given (1) at the specific Antarctic Peninsula overpasses of AIRS for the Antarctic Peninsula nest and (2) hourly during the whole

325 period of the mountain wave event. NAT PSCs are simulated using a size distribution based on van den Broek et al. (2004), shown in Fig. 3. We prescribe H_2SO_4 in the lower stratosphere (Thomason et al., 2008; SPARC, 2013) in the global domain. In the nested domains, H_2SO_4 runs freely after initialised by the parent domain.

4 Satellite datasets

4.1 CALIOP

330 The Cloud-Aerosol LIdar with Orthogonal Polarisation (CALIOP, Pitts et al., 2009; Höpfner et al., 2009; Pitts et al., 2018) onboard the Cloud-Aerosol Lidar and Infrared Pathfinder Satellite Observation (CALIPSO) was launched on 28 April 2006 (Winker et al., 2007). In 2008, the satellite flew as part of NASA's A-train constellation in an orbit with $98°$ inclination at an altitude of $705\,km$ (Stephens et al., 2002; Pitts et al., 2018). Its orbit was sun-synchronous with equator crossings at about 01:30 and 13:30 LT. It measured down to $82°S$ with a repeat cycle of 16 days. In February 2018, it was moved to a lower orbit.

335 CALIOP is a light detecting and ranging (Lidarlidar) instrument, set up in nadir geometry. It scans the atmosphere at wavelengths of 532 and $1064\,nm$ with parallel and orthogonal polarisations for the 532-nm channel (Winker et al., 2007). In altitudes from 8.4 to $30\,km$, the vertical resolution is $180\,m$ or higher. Horizontal averaging of $5\,km$ is applied for the detection of PSCs with CALIOP (Pitts et al., 2018). At the Earth's surface, the light beam has a diameter of about $100\,m$ (Höpfner et al., 2009; Pitts et al., 2018).

340 For the detection of PSCs, a combination of two values is used (Pitts et al., 2018): (1) the ratio of total and molecular backscatter coefficient R_{532} and (2) the backscatter coefficient at perpendicular polarisation $\beta_{532}\beta_\perp$, both at a wavelength of $532\,nm$. Discrimination of the PSC types can be seen in diagrams of R_{532} vs. $\beta_{532}\beta_\perp$. Different regions in this diagram refer to the different PSC types (see Pitts et al., 2018). categories: STS, NAT mixtures, enhanced NAT mixtures, Ice and Wave-ice (see Pitts et al., 2018). The thresholds to distinguish PSCs from background noise are calculated as daily median

345 plus one absolute standard deviation and depend on potential temperature ($\beta_{\perp,thres}$ and $R_{532,thres}$). The boundary between the NAT mixtures and ice ($R_{NAT|ice}$) is calculated dynamically depending on the state of dehydration and denitrification (Pitts et al., 2018).

We use the PSC climatology of Pitts et al. (2018), which is the version 2 level 1B data, averaged with a window of along the satellite path. It is restricted to night-time southern hemispheric data during the mountain wave event (data is available within

350 the time frame we are interested in from 22 to 29 July 2008). We examine the altitude levels between 15 and 30 km ~~that are relevant for formation of PSCs on the one hand and exclude tropospheric clouds on the other hand~~where (1) no tropospheric clouds contaminate the results and (2) most of the PSCs can be found (see, e.g., Fig. 13 of Pitts et al., 2018). In addition, the dataset includes temperature and pressure data of Modern-Era Retrospective analysis for Research and Applications version 2 (MERRA2, Gelaro et al., 2017), which originally has a horizontal resolution of $0.5° \times 0.625°$, interpolated on the CALIOP

355 paths.

4.2 AIRS

The Atmospheric InfraRed Sounder (AIRS, Aumann et al., 2003; Chahine et al., 2006) is one of the instruments onboard the Aqua satellite, which was launched in May 2002 and which is part of the A-train constellation right ahead of CALIPSO. Thus, its orbit is the same as CALIPSO in 2008 but about 1 to 2 min ahead of CALIPSO[1].

360 The AIRS instrument is a nadir sounder with across-track scanning capabilities that scans the atmosphere by 90 footprints per scan with a ground coverage of 1780 km and a size of 13.5×13.5 km^2 (nadir) to 41×21.4 km^2 (scan edge) per footprint (e.g., Orr et al., 2015; Hoffmann et al., 2017). It measures the spectrally resolved radiances in wavelengths between 3.74 and 15.4 µm. Brightness temperatures in the 15 µm band can be used to derive information about gravity waves in the lower polar stratosphere (Hoffmann et al., 2017). In this study we use a data product averaging over 21 channels around 15 µm to

365 improve the signal-to-noise ratio (Hoffmann et al., 2017). The temperature weighting function in this band peaks at an altitude of around 23 km with a full width at half maximum of 15 km and with information from the altitude range between 17 and 32 km. Therefore, it is well suited to derive information about gravity waves in the altitude region where PSCs are expected to exist.

~~In this study, this~~ This band is used to examine the mountain wave event at the Antarctic Peninsula mentioned above. The

370 same algorithm as in previous studies is used to compare the model data with specific Antarctic Peninsula overpasses of AIRS (Hoffmann and Alexander, 2010; Hoffmann et al., 2016, 2017). In particular, the ICON-ART data are resampled on the AIRS measurement grid and a radiative transfer model is used to simulate AIRS measurements based on the ICON-ART data to allow for a direct comparison with the real observations.

5 ~~Mountain-wave induced~~ Mountain-wave-induced PSCs with ICON-ART

375 In this study, we investigate a mountain wave event during July 2008 with ICON-ART in a configuration with interactive chemistry and local grid refinement around the Antarctic Peninsula. This section comprises an evaluation of the dynamical structure of the mountain wave (Sect. 5.1) ~~,~~ and comparisons of the model results with CALIOP and AIRS measurements (Sect. 5.2 and Sect. 5.3)~~and~~. In addition, it discusses the impact of the direct simulation of ~~mountain-wave induced~~ mountain-wave-induced PSCs on the polar ozone chemistry (Sect. 5.4).

---

[1]https://www-calipso.larc.nasa.gov/about/atrain.php, last access ~~05 November 2020~~19 March 2021
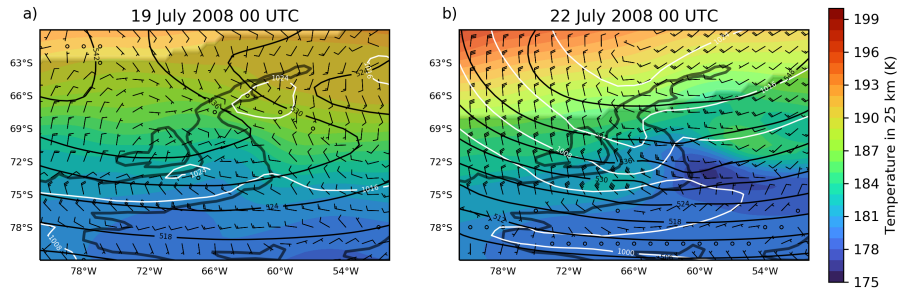
Figure 4. Meteorological situation at the Antarctic Peninsula for a) 19 and b) 22 July 2008 at 00 UTC from ERA-Interim. The colours depict temperature at about $25\,\mathrm{km}$ in K. The white lines correspond to the mean sea level pressure in hPa. The black lines are geopotential heights at $500\,\mathrm{hPa}$ in gpdam. The wind barbs depict the surface wind in knots. The dark shadow shows the air masses within the polar vortex, determined according to Nash et al. (1996) on $\theta = 475\,\mathrm{K}$. Panels covering the whole period of the mountain wave event can be found in the supplement.

5.1 Dynamical structure of the mountain wave ~~on 22 July 2008~~

The evolution of the ozone loss and the Antarctic polar vortex in 2008 was comparable to the previous years although the so-called ozone hole lasted rather long into December (Tully et al., 2011). It was a year with increased gravity wave activity at the Antarctic Peninsula (Hoffmann et al., 2016). We chose a gravity wave event lasting ten days from 19 July until 29 July 2008 with lowest temperatures during the whole winter season (Noel and Pitts, 2012). By end of July 2008, the polar vortex was close to its maximum extension whereas the stratospheric ozone concentration started to decrease (Tully et al., 2011).

Figure 4 summarises the meteorological conditions around the Peninsula, based on the ERA-Interim reanalysis. It shows several variables at the beginning of the mountain wave event on 19 July 2008 (panel a) and at its peak stratospheric dynamics on 22 July 2008 (panel b). Panels covering the whole event can be found in the supplement (Figure S1).

The Antarctic Peninsula was located at the vortex edge during the whole mountain wave event, as depicted by the shadowed regions in the panels and determined by the method by Nash et al. (1996). Starting from 19 July 2008, an approaching high pressure system led to increase of the mean sea level pressure gradient (white lines) at the Antarctic Peninsula with corresponding increase of easterly winds at the mountain range. The gradient on the geopotential height at $500\,\mathrm{hPa}$ (black lines) also increased showing the large-scale easterly flow in this altitude on 22 July. This led to temperatures as low as $175\,\mathrm{K}$ at the altitude of about $25\,\mathrm{km}$ (colours-coded) in the lee of the mountain as a result of the generated mountain wave. In the following, we will focus our analysis of the mountain event at its peak on 22 July 2008.

Figure 5 shows cross sections of the mountain wave dynamics along the line shown in Fig. 2 for the example of 22 July 2008 at 04 UTC in the altitude range between 12 and $30\,\mathrm{km}$. The model data is interpolated to the path by an inverse distance method including the three neighboured grid points.
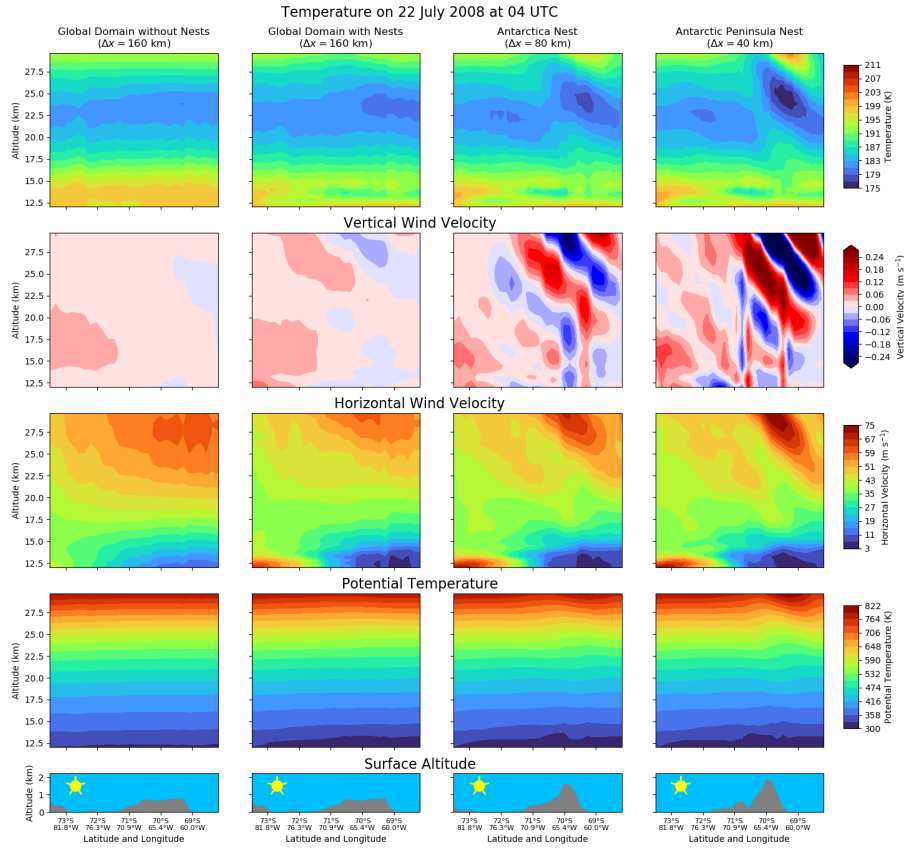
Figure 5. Cross sections on 22 July 2008 at 04 UTC along the white line in Fig. 2. Each row represents a different variable in the model. The bottom row shows the surface altitude with the Antarctic Peninsula at around $65°$W. The columns represent the different simulations and domains: The first column is the simulation without nests ($\Delta x \approx 160\,\mathrm{km}$), the second one is the global domain ($\Delta x \approx 160\,\mathrm{km}$) including two-way nesting and the two right columns represent the Antarctica ($\Delta x \approx 80\,\mathrm{km}$) and Antarctic Peninsula nests ($\Delta x \approx 40\,\mathrm{km}$), respectively. The dynamical variables temperature, vertical wind velocity, horizontal wind velocity and potential temperature are shown in this figure.

~~This figure demonstrates that the mountain wave can be directly simulated with the resolution of .~~ The left column shows the simulation without nests whereas the three other columns illustrate the dynamics in the different domains shown in Fig. 2 of the simulation with the nests.

The bottom row of Fig. 5 shows the resolution of the Antarctic Peninsula ~~which is a crucial parameter for simulating mountain-wave induced PSCs as it determines the flow over the mountain range~~ in the different domains. As can be seen, ~~in the global domains with resolution of the top of~~ the higher the horizontal resolution the better the Antarctic Peninsula ~~does not exceed . Therefore,~~ can be represented as mountain range. Thus, this indicates that the flow over the mountain ~~range is underrepresented in the model. By increasing the resolution, however, to the height of the Antarctic Peninsula peaks at around and can be represented as mountain range with associated directly simulated flow over the orography~~ in the Antarctic Peninsula nest is improved with respect to the global resolution of 160 km.

This is reflected in the variables shown in Fig. 5. Temperatures as low as 175 K only occur in the Antarctic Peninsula nest with a 40 km resolution in the lee of the mountain. ~~In addition, it~~ These temperatures are in agreement with ERA-Interim (see Fig. 4). The temperature in the Antarctic Peninsula nest also shows the characteristic high and low temperature patterns as calculated by theory (e.g., Queney, 1947) and seen by measurements (e.g., Wright et al., 2017). The temperature perturbation in the order of 10 K is consistent with previous studies of mountain waves (Meilinger et al., 1995; Carslaw et al., 1998a; Eckermann et al., 2009).

The horizontal wavelength of the simulated mountain wave is in the order of 300 km, which is a medium-large wavelength compared to other events (see e.g., Alexander and Teitelbaum, 2007; Plougonven et al., 2008; Hoffmann et al., 2014). In addition, the vertical resolution is in the order of 500 m at least in the lower parts of Fig. 5. This is why the mountain wave can be captured by the resolution of 40 km in the Antarctic Peninsula nest.

The relatively large temperature gradients in the Antarctic Peninsula nest are also in agreement with gradients in the wind velocities which are shown in the second and third row of Fig. 5. In the lee of the Antarctic Peninsula, the vertical wind velocity changes signs in altitudes where the temperature increases or decreases and has maximum values above $0.3\,\mathrm{m\,s^{-1}}$. Largest horizontal wind velocities in the order of $75\,\mathrm{m\,s^{-1}}$ occur in altitudes above 27 km.

The mountains also cause perturbations in the potential temperature (~~forth~~ fourth row in Fig. 5) in the lee. If diabatic processes are negligible, the flow follows the contours of potential temperature which will be shown in the PSC precursors in Sect. 5.4.2.

Up to now, it was only demonstrated that ~~mountain waves are~~ this mountain wave event can be directly simulated in the Antarctic Peninsula nest (right column) and ~~are~~ is consistent with the theory of mountain waves. In addition, Figure 5 also shows the impact of the two-way nesting in ICON-ART. The nest around the Antarctica with resolution of about 80 km (third column) interacts with both nests and shows the transition between these resolutions. The mountain wave at the Antarctic Peninsula cannot be represented adequately in the resolution of 160 km in the simulation without the nests (left column in Fig. 5). The characteristic wave patterns do not occur in this simulation. In contrast to this, the global domain in the simulation with the nests (second column in Fig. 5) shows a decrease in temperature of about 2 K in the lee of the mountains~~as~~. This is a result of the two-way nesting and the lower temperature due to the directly simulated mountain wave in the Antarctic Peninsula

nest. ~~Of course, the~~ The amplitude is lower than it is expected by mountain waves but the effect of the mountain wave is still remarkable also in the global grid of $160\,\mathrm{km}$ resolution.

This is also visible in the other variables of Fig. 5. Especially for the vertical wind velocity (second row), one can see that wave-like structures occur in the global domain where they cannot be represented without the nests. Therefore, we can expect that ~~mountain-wave induced~~ mountain-wave-induced PSCs can also be represented in this relatively low global resolution because they are directly simulated in the locally refined regions. Before the impact on other variables in the model is analysed, PSCs and mountain waves are compared to CALIOP and AIRS for the mountain wave event in the next sections.

5.2 Comparison of simulated PSCs with CALIOP measurements

For a comparison with CALIOP, the ICON-ART PSC volume concentrations ~~of the Antarctic Peninsula nest~~ are interpolated (1) horizontally by an inverse distance method, (2) linearly in time and (3) linearly in geometric altitude to all CALIOP paths from 22 to 29 July 2008 where CALIOP's orbit was within the region of Antarctic Peninsula nest. Details about the interpolation can be found in Weimer (2019, Sect. 4.7.4).

As pointed out by previous studies, an adequate comparison of CALIOP with model data can only be set up if the model data is transferred into the optical space measured by CALIOP at $532\,\mathrm{nm}$ ~~using~~ . We apply the method by Engel et al. (2013), Tritscher et al. (2019) and ~~?, which we apply here~~ Steiner et al. (2021). It is based on T-matrix and Mie calculations (e.g., Mishchenko et al., 1996) with particle number densities and particle radii of the PSC types as input ~~and parallel as well as perpendicular backscatter coefficients and backscatter ratio as output~~. The external PSC mixtures of ICON-ART are combined to optical properties (R_{532} and $\beta_{\perp}$) for each grid point. In accordance with Tritscher et al. (2019) and ~~?~~ Steiner et al. (2021) we use aspect ratios of ice and NAT of 0.9 and refractive indices of 1.44 for STS (Krieger et al., 2000), 1.31 for ice and 1.48 for NAT (Middlebrook et al., 1994).

~~As described in Pitts et al. (2018), the~~ The three thresholds to determine the boundaries between ~~STS, NAT and ice are dynamically calculated depending on the measured values. Like in ?, we calculate the thresholds in the backscatter ratio ($R_{532,\mathrm{thres}}$~~ the PSC categories are taken from the measurement data and averaged daily for each CALIOP height level ($\overline{\beta}_{\perp,\mathrm{thres}}$, $\overline{R}_{532,\mathrm{thres}}$ and $\overline{R}_{\mathrm{NAT|ice}}$) (Tritscher et al., 2019; Steiner et al., 2021). As pointed out by Engel et al. (2013), it is important to account for the measurement uncertainties σ_R and $\sigma_{\beta,\perp}$ to compare the simulated R_{532} and $\beta_{\perp}$ with CALIOP. These uncertainties are calculated according to Eqs. (5) and ~~perpendicular backscatter coefficient ($\beta_{\perp,\mathrm{thres}}$) as daily means from data in the Antarctic Peninsula nest. We add the measurement uncertainty to these thresholds to determine the PSC types as statistical outliers as in the measurements based on Engel et al. (2013) and Tritscher et al. (2019). Finally, the backscatter ratio threshold between NAT and ice ($R_{\mathrm{NAT,ice}}$) depends on the concentrations of gaseous~~ (6) of Tritscher et al. (2019), respectively. The simulated R_{532} and ~~, thus on the state of denitrification and dehydration. We use the average threshold of 2.75 suggested by Pitts et al. (2018) because the data structure is similar in space as well as in time to the data used for Fig. 5b of Pitts et al. (2018)~~ $\beta_{\perp}$ are scaled by a normal distribution with mean at the simulated value and standard deviation as the respective σ. To

summarise, the condition to determine if a PSC is detected is then

$$\beta_{\text{scal}} > \overline{\beta}_{\perp,\text{thres}} + \sigma_{\beta,\perp}, \quad \beta_{\text{scal}} \sim \mathcal{N}(\beta_\perp, \sigma^2_{\beta,\perp}) \tag{1}$$

or

$$R_{532,\text{scal}} > \overline{R}_{532,\text{thres}} + \sigma_R, \ R_{532,scal} \sim \mathcal{N}(R_{532}, \sigma^2_R) \tag{2}$$

470 ~~Statistical analysis of PSC occurrence for a) ICON-ART simulation and b) CALIOP measurements in the Antarctic Peninsula nest. The ICON-ART data is interpolated to the CALIOP paths in the altitude range from to in the nest in the time range between 22 and 29 July 2008 where CALIOP data is available. The colours correspond to the numbers in the circles and show the fraction of the PSC type that is present in the temperature bins with a width of . The sizes of the circles correspond to the total number of grid points with PSCs in the temperature bins relative to the maximum in each panel, also denoted at the right~~

475 ~~hand side of the panels. The temperature data for CALIOP originates from MERRA2, which is part of the CALIOP product.~~

~~Since the nested simulation is~~ Since the ICON-ART simulations are free-running we cannot expect the PSCs to occur at exactly the same locations as in the measurements. Therefore, we compare the ~~development~~ evolution of PSCs with respect to the temperature in both ~~datasets~~CALIOP and ICON-ART, which is a crucial parameter in the formation of PSCs (e.g., Solomon, 1999). We count the occurrence of the different PSC ~~types~~categories by the method described above in temperature

480 bins and compare them between ICON-ART and CALIOP.

~~The results can be found in Fig. 6. It~~The "No" PSC category is neglected in this comparison to emphasise the occurrence of PSCs in the temperature bins. The data is restricted to the region of the Antarctic Peninsula nest resulting in a total number of about one million grid points with PSCs for CALIOP and about 0.5 million grid points with PSCs in ICON-ART. This large difference could either be a result of horizontal shifted PSCs especially in the later part of the free-running simulation or a

485 problem with the constant number concentrations used in the model. It should be further analysed in the future.

Figure 6 shows the relative number of grid points (in %) on the CALIOP paths where the different PSC ~~types~~categories occur. The ~~"No" PSC category is obviously the dominant category for both ICON-ART and CALIOP, but neglected in this comparison to see only the occurrence of PSCs in the temperature bins.~~

~~In Figure 6, the~~size of the circles correspond to the total number of grid points with PSCs ~~, that is also printed on the right~~

490 ~~hand side of the panels,~~and the colour of the circles show the relative number of this PSC ~~type~~category occurrence in the respective temperature bin. The panels show the PSC occurrence in a) the simulation without the nests, b) in the Antarctic Peninsula nest and c) in the CALIOP measurements. For ICON-ART (~~panel a~~panels a and b), the modelled temperatures are used directly~~whereas the~~. The temperature for CALIOP (panel ~~b~~c) is interpolated from MERRA2 and provided as part of the original dataset (Pitts et al., 2018).

495 As can be seen, ~~ice particles dominate the existence of PSCs in the lowest temperature bins of and for both ICON-ART and CALIOP.~~ the relative distribution of grid points with PSCs coincides in all panels down to a temperature of about 180 K. Temperatures lower than that, however, are underrepresented in the simulation without the nest, compared to CALIOP. This is expected from Fig. 5 since temperatures are higher than 180 K in the simulation without nests in the lee of the
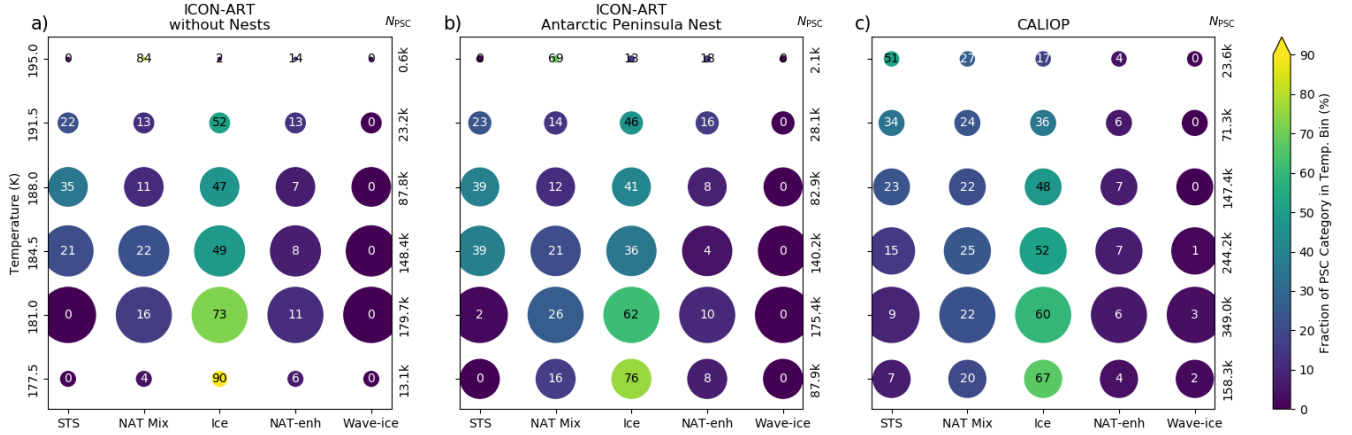
Figure 6. Statistical analysis of PSC occurrence for a) the ICON-ART simulation without nests, b) the ICON-ART simulation with nests in the Antarctic Peninsula nest and c) CALIOP measurements. The data is restricted to the region of the Antarctic Peninsula nest for all panels to get comparable results. The ICON-ART data is interpolated to the CALIOP paths in the altitude range from 15 to 30 km in the nest in the time range between 22 and 29 July 2008 where CALIOP data is available. The colours correspond to the numbers in the circles and show the fraction of the PSC category that is present in the temperature bins with a width of 3.5 K. The sizes of the circles correspond to the total number of grid points with PSCs in the temperature bins relative to the maximum in each panel, also denoted at the right hand side of the panels as N_{PSC}, following the nomenclature by Spang et al. (2016). The "k" behind the numbers abbreviate thousand, i.e. 179.7k = 179700 grid points with PSCs. The temperature data for CALIOP originates from MERRA2, which is part of the CALIOP product.

mountains. In addition, the ~~"NAT-enh" category is negligible for both datasets. The development of pure STS particles is~~
~~similar between ICON-ART and CALIOP , although the fractions are underestimated at high temperatures. However, the~~
~~number of measurements in this bin is small compared to the other ones so that this statistic could be non-significant. Whereas~~
~~NAT particles in the "NAT Mix" category exist over the whole temperature range with a similar~~ simulation without nests
overestimates the fraction of the ice category at temperatures lower than 183 K compared to CALIOP.

Both deficiencies are improved in the Antarctic Peninsula nest with resolution of 40 km (panel b). PSCs in the ice category occur with a similar fraction like in CALIOP in the 181 K bin and the relative number of grid points with PSCs in the lowest temperature bin coincides with the measurements. The fractions of the NAT mixtures and NAT enhanced categories are also comparable to CALIOP over the whole range of temperatures. For medium temperatures (188 and 184.5 K) the fraction of the STS category is slightly overestimated compared to CALIOP. A reason for this could be missing fine structures in the gravity wave, discussed in the next section. The fraction of the ice category is 9 % larger in the lowest temperature bin than in CALIOP.

Comparing the three panels of Fig. 6, there seems to be a resolution-dependent shift of overestimated fraction in the ~~measurements, their existence is cut off at temperatures lower than about~~ ice category. At the resolution of 160 km, the ~~lower boundary of the bin. This is due to the used operator splitting and will be further investigated in Sect. 5.4.~~ overestimation starts
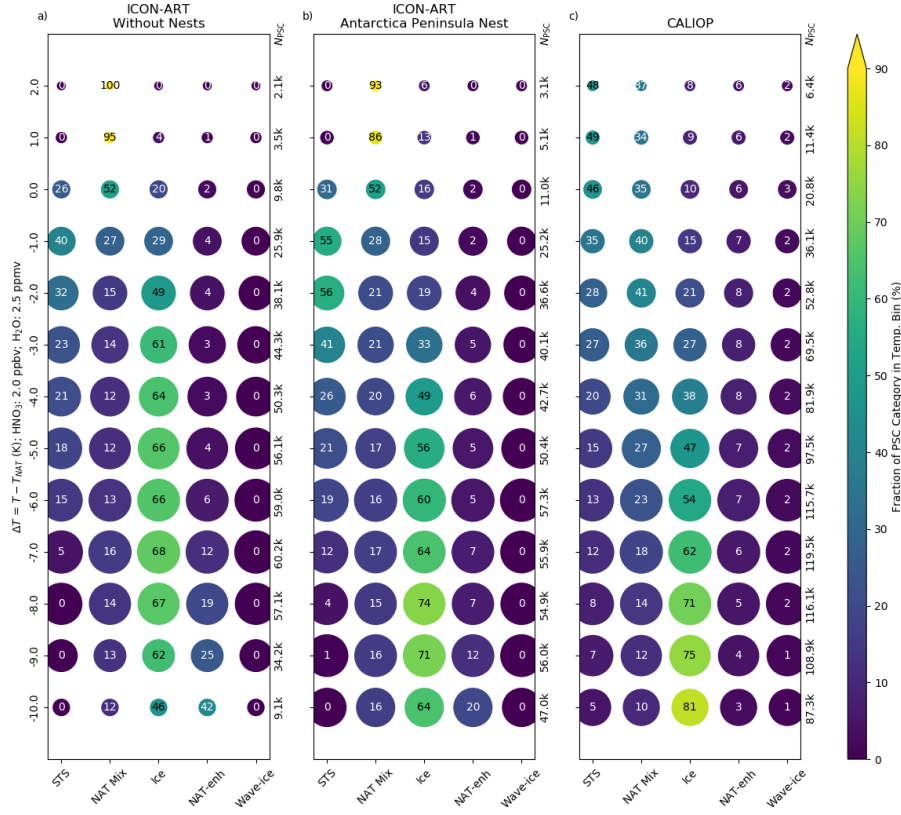
Figure 7. ~~Statistical analysis of PSC occurrence for a) ICON-ART simulation and b) CALIOP measurements~~ Same as Fig. 6, but relative to T_{NAT}. Here, a common T_{NAT} for both ICON-ART and CALIOP y-axes is derived from Hanson and Mauersberger (1988) with input of ~~$X_{H_2O} = 5\,ppmv$~~ $X_{H_2O} = 2.5\,ppmv$ and ~~$X_{HNO_3} = 10\,ppbv$~~ $X_{HNO_3} = 2\,ppbv$ based on Tritscher et al. (2019). The data are binned in terms of temperature difference with a bin width of $1\,K$. ~~Apart from that, the structure is the same as in Fig. 6.~~

at the $181\,K$ bin, for $40\,km$ it begins at $177.5\,K$. Thus, this figure suggests that even a higher resolution is needed to get PSC
515   distributions at low temperatures comparable to CALIOP. This is consistent to previous studies with mesoscale models that used a higher resolution to study mountain waves (e.g., Noel and Pitts, 2012).

~~In addition to the analysis of direct temperature as reference, we also analyse the development of PSCs in~~ This shift in the fraction of the ~~same manner relative to~~ ice category is emphasised in Figs. 7 and 8. They show the evolution of the PSC categories relative to the NAT and ice formation temperatures, T_{NAT} ~~(Fig. 7)~~ and T_{ice} ~~(Fig. 8), calculated with~~
520   ~~$X_{H_2O} = 5\,ppmv$ and $X_{HNO_3} = 10\,ppbv$ as input. We chose these constant values because the mixing ratios measured by Microwave Limb Sounder (MLS), also provided as part of the CALIOP product, only include the gaseous part of and which leads to inconsistencies when knowing that PSCs exist in CALIOP. Nevertheless, this analysis includes the pressure dependence of the~~. We calculated these temperatures with $X_{H_2O} = 2.5\,ppmv$ and $X_{HNO_3} = 2\,ppbv$ based on the formulas by Hanson and Mauersberger and Marti and Mauersberger (1993), respectively, to get a comparable pressure-dependent reference temperature for both the
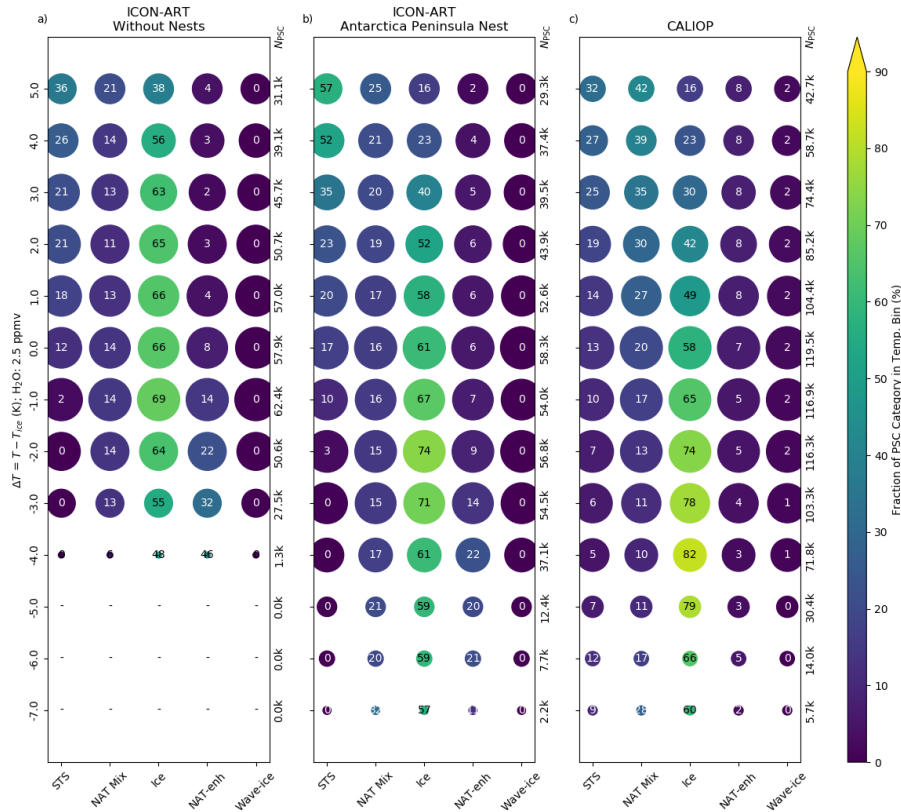
Figure 8. ~~Statistical analysis of PSC occurrence for a) ICON-ART simulation and b) CALIOP measurements~~ Same as Fig. 6, but relative to T_{ice}. Here, a common T_{ice} for ~~both~~ ICON-ART and CALIOP y-axes is derived from Marti and Mauersberger (1993) with input of ~~$X_{\text{H}_2\text{O}} = 5\,\text{ppmv}$~~ $X_{\text{H}_2\text{O}} = 2.5\,\text{ppmv}$ based on Tritscher et al. (2019). The data are binned in terms of temperature difference with a bin width of $1\,\text{K}$. ~~Apart from that, the structure is the same as in Fig. 6.~~

525   model and the measurements. These constant volume mixing ratios are used only to calculate the PSC existence tempera-
tures ~~so that it provides more realistic thresholds for the existence temperatures than constant values like and~~. They are based
on satellite measurements shown by Tritscher et al. (2019) for late July, accounting for denitrification and dehydration.

~~Although~~ As can be seen in Fig. 7, the number of grid points ~~is relatively low for temperatures around~~ with PSCs grows when
the temperature gets lower than T_{NAT} ~~and higher in Fig. 7, no ice PSCs exist in both simulation (panel a) and measurements~~
530   ~~(panel b). The major fraction in this temperature region is accounted to the "NAT mix" category in both panels although PSCs~~
~~usually do not exist. In total, the number of data points in ICON-ART is higher for $T > T_{\text{NAT}}$ and lower for $T < T_{\text{NAT}}$ in~~
~~comparison~~ in all three panels. Similar patterns as in Fig. 6 can be seen: Overestimation of the STS category at temperatures
around 1 to ~~CALIOP. However, the principal development is similar to CALIOP: at temperatures about lower than T_{NAT} ice~~
~~PSCs begin to form and turn out to be the major fraction of all PSC types. As already mentioned in the description of Fig. 6,~~
535   ~~NAT PSCs are cut off at a certain point, which will be investigated later in this study.~~

~~The upper part of Fig 8, which shows the PSC development relative to~~ 3 K lower than T_{NAT} in the Antarctic Peninsula nest and differences in the ice category. In case of the simulation without nests, the fractions of ice are larger than in CALIOP for $\Delta T_{\mathrm{NAT}} < 0\,\mathrm{K}$. In the Antarctic Peninsula nest, this overestimation can be seen at temperatures $\Delta T_{\mathrm{NAT}} < -2\,\mathrm{K}$.

The comparison with respect to T_{ice} ~~, corresponds to the lower part of Fig. 7 with a shift of about . In accordance to the measurements,~~ in Fig. 8 emphasises the previous findings. In the simulation without the nests, temperatures lower than $\Delta T_{\mathrm{ice}} = -3\,\mathrm{K}$ are underrepresented compared to CALIOP. The fraction of the ice category peaks with 69 % at $\Delta T_{\mathrm{ice}} = -1\,\mathrm{K}$. The resolution of 40 km in the Antarctic Peninsula nest is able to reproduce the general evolution of PSCs for $\Delta T_{\mathrm{ice}} < -3\,\mathrm{K}$, but the fraction peaks with 74 % at $\Delta T \mathrm{ice} = -2\,\mathrm{K}$. In contrast, the CALIOP measurements suggest that the fraction of ~~ice PSCs in ICON-ART start to dominate at temperatures lower than T_{ice} with fractions larger than . The largest fractions occur at temperatures about to lower than T_{ice} in both ICON-ART and CALIOP~~the ice category should be larger for $\Delta T_{\mathrm{ice}} < -2\,\mathrm{K}$. Most probably, an even higher resolution is needed to reflect ice PSCs at these temperatures.

Although ~~we will show in the next sections that mountain-wave induced PSCs can be directly simulated~~Fig. 5 suggested that main parts of the mountain wave can be captured in the Antarctic Peninsula nest, no PSCs in the "Wave-ice" ~~PSCs~~ category are simulated by ICON-ART. As ~~shown in Eq.~~ mentioned in Sect. 2, the ice particle number concentration is essentially set to the constant value of $0.25\,\mathrm{cm}^{-3}$ in the stratosphere. The ice number concentration in mountain waves can increase to values of a few cm^{-3} and then ~~leading~~ lead to larger backscatter ratios ~~(e.g., Engel et al., 2014)~~(e.g., Engel et al., 2013). Therefore, this too low ice number concentration could explain why the backscatter ratio to determine the PSC ~~types~~ categories does not get as large as 50 which is needed for the "Wave-ice" category (Pitts et al., 2018).

In total, ~~we showed in this section that, apart from some differences in NAT at low temperatures and the "Wave-ice" category, the general formation of PSCs~~ this section demonstrated that the PSC scheme in ICON-ART is able to generate PSCs similar to CALIOP. The peak fraction of the ice category seems to move to lower temperatures if the resolution is increased, suggesting that an even higher resolution is needed to capture the ice formation at the lowest temperatures. On the other hand, this analysis demonstrated that the evolution of the PSCs is clearly improved in the Antarctic Peninsula nest with respect to ~~different reference temperatures is similar to the CALIOP~~measurements. ~~Therefore, we will show the development of mountain-wave induced PSCs in the next sections qualitatively but a quantitative comparison is difficult because of the too large particle number concentration of ice PSCs~~CALIOP. Some differences in the STS category with respect to CALIOP also indicate that some fine structures of the mountain wave are missing, which is discussed in the next section.

5.3 Direct simulation of mountain waves compared to AIRS

For the comparison with AIRS, temperature and pressure of ICON-ART in the Antarctic Peninsula nest is saved at the time step closest to each of the AIRS overpasses during 20 and 21 July 2008. These data are then convolved with the same temperature weighting functions that apply for the AIRS observations (see e.g., Hoffmann et al., 2017). The resulting brightness temperature (BT) perturbations can be found in Fig. 9 on 20 July and in Fig. 10 on 21 July 2008 for AIRS and ICON-ART.

Horizontal structures of the BT perturbations are shown in the first and second columns for AIRS and ICON-ART, respectively. Largest perturbations are present directly above the Antarctic Peninsula for both AIRS and ICON-ART which
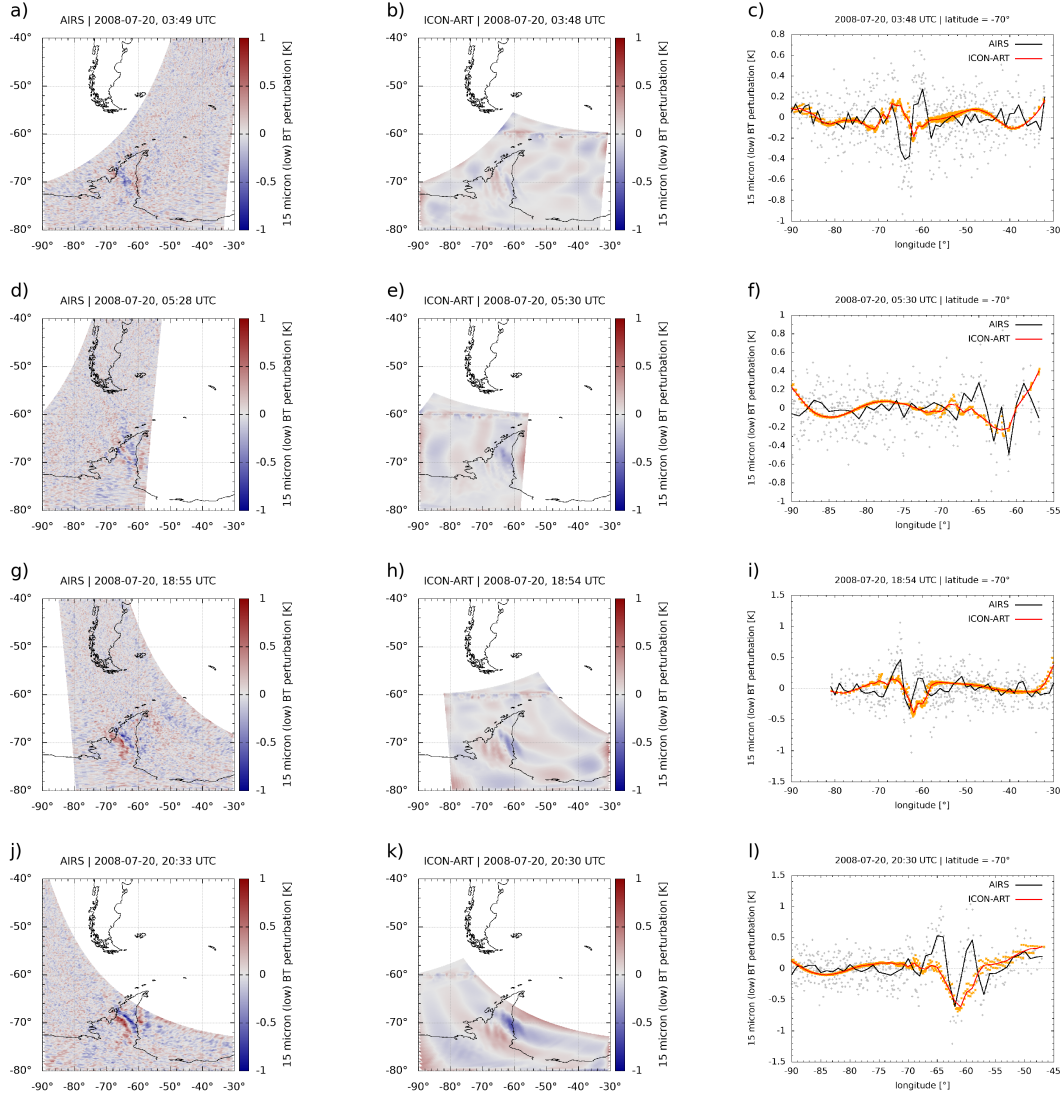
Figure 9. Comparison of AIRS and ICON-ART brightness temperature (BT) perturbations at wavelengths of 15 μm for all Antarctic Peninsula overpasses of AIRS during 20 July 2008. The first column shows the BT perturbation observed by AIRS, the second column the simulated perturbation based on ICON-ART in the Antarctic Peninsula nest. The third column shows the perturbation for AIRS (black) and ICON-ART (orange) at a latitude of 70 °S. The rows show different overpasses at (a-c) 03:49 UTC, (d-f) 05:28 UTC, (g-i) 18:55 UTC and (j-l) 20:33 UTC.
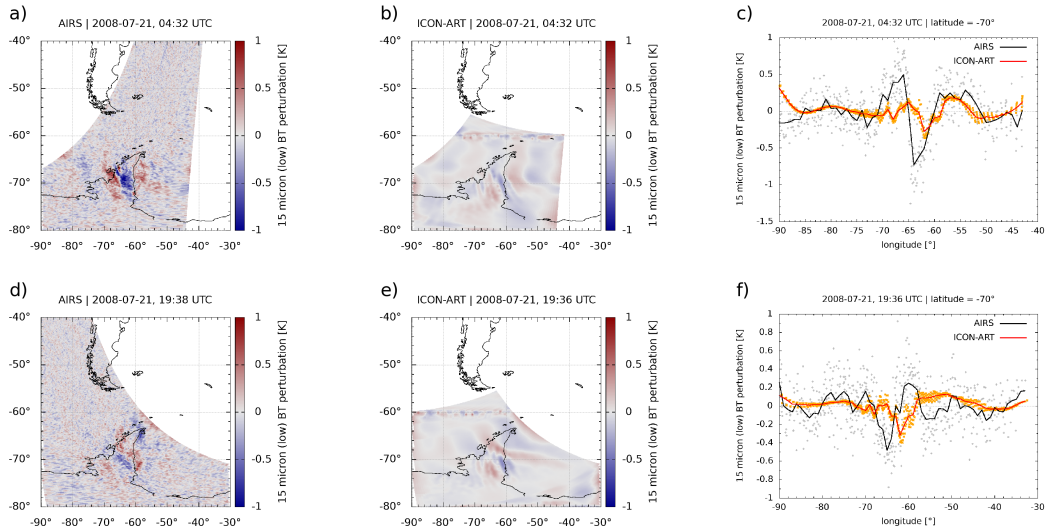
Figure 10. Same as Fig. 9 but for 21 July 2008. The rows show different overpasses at (a-c) 04:32 UTC and (d-f) 19:38 UTC.

demonstrates that the perturbations originate from mountain waves propagating into the lower stratosphere. In addition, the mountain wave has an angle with respect to the Antarctic Peninsula mountains of about $45°$ ~~suggesting a horizontal wind from south west. This is also represented in the~~ , represented in both AIRS and ICON-ART~~simulation~~.

Fine structures as e.g. in panel j of Fig. 9 cannot be simulated in this simulation setup of ICON-ART (e.g. panel k) since the resolution of $40\,\mathrm{km}$ is still too coarse to predict them. ~~Thus, some fine structures are missing in the ICON-ART simulation but the general behaviour of the mountain wave can be directly simulated in the Antarctic Peninsula nest~~, which was already indicated by the comparison to CALIOP. A higher resolution would be needed to capture these fine structures, see e.g. Orr et al. (2015). The chemistry non-linearly depends on temperature which means that small temperature variations could have a measurable effect on the chemistry (e.g., Murphy and Ravishankara, 1994). As pointed out previously, the microphysics of PSCs is one example for this. If the amplitude is underestimated, like in Fig. 9b and c, a higher resolved model would most probably generate more ice PSCs, thus improving the CALIOP comparison at the lowest temperatures.

~~This is~~ These results are also stressed by the comparison of the perturbations at the latitude of $70\,°\mathrm{S}$ that are shown in the third column of Figs. 9 and 10. The largest BT perturbations can be found at the longitude of the Antarctic Peninsula in all the panels. Some fine structures are missing in ICON-ART. For instance, at some overpasses the amplitude of the wave is underestimated compared to AIRS (e.g. panel c of Fig. 10). At other overpasses, the phase of the wave is shifted with respect to AIRS, as e.g. in panels c of Fig. 9 and f in Fig. 10. This is most probably a result of the free-running simulation where the wave cannot be expected to be located at exactly the same location as in the measurements.
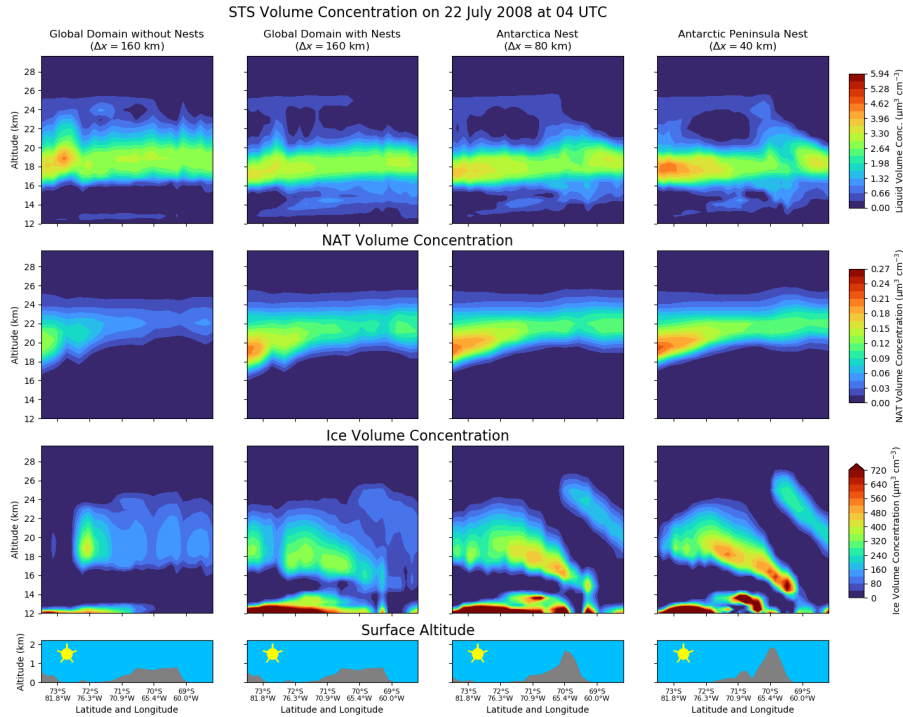
Figure 11. Same as Fig. 5 but for the volume concentrations of the different PSCs: ~~STS~~liquid aerosol, NAT and ice. Please note the different colour bars.

In total, we have shown in this section that, apart from some missing fine structures, the mountain wave event taking place in the end of July 2008 can be represented with the resolution of $40\,\mathrm{km}$ in comparison with AIRS.

5.4 Impact of ~~mountain-wave induced~~ mountain-wave-induced PSCs on the chemistry

590 In the previous sections, it was demonstrated that both the PSC formation and the formation of the mountain wave are in relatively good agreement with measurements considering the limits in measurements and simulation setup. In this section, we investigate the impact of directly simulated ~~mountain-wave induced~~ mountain-wave-induced PSCs on the interactively calculated chemistry in ICON-ART.

5.4.1 The formation of PSCs in the mountain wave

595 Figure 11 demonstrates that the ICON-ART model has the potential to close the gap between direct simulations of ~~mountain-wave induced~~ mountain-wave-induced PSCs and their treatment in relatively coarse global resolutions ~~can be closed by ICON-ART. The STS volume concentration~~. The volume concentration of liquid particles (first row) in the global domain with nests is influenced by the mountain wave, especially at altitudes higher than $20\,\mathrm{km}$ where particle volume concentrations close to zero occur in the global domain which do not exist without the nesting technique. The influence of the mountain wave on ~~STS~~ liquid

aerosol is amplified within the nests. The ~~STS~~ liquid particles are assumed to freeze at temperatures $3\,\mathrm{K}$ below the frost point (Carslaw et al., 1995; Koop et al., 2000). Thus, ~~STS~~ liquid particles are only computed for higher temperatures so that ~~STS particles~~ they are formed in the mountain wave where the temperature is higher than this threshold.

STS and NAT compete with each other in taking up HNO_3. This is why in this case study distinct layers exist: NAT PSCs at altitudes higher than $20\,\mathrm{km}$ and STS PSCs at lower altitudes where also H_2SO_4 is enhanced~~.~~, see Sect. 5.4.2. The NAT volume concentrations are increased in the Antarctic Peninsula nest (second row, right column) which is why they are also increased in the global domain ~~in the simulation with the~~ comparing the simulations with and without nests.

In contrast to the literature (e.g., Carslaw et al., 1999; Svendsen et al., 2005), the NAT volume concentration decreases when the air masses approach the mountain wave. Since the NAT size bins are advected with the general air masses, the wave-like patterns occur in both nests. As a result of the operator splitting used in ICON-ART, the largest fraction of gaseous H_2O leads to ice formation at temperatures lower than about $180\,\mathrm{K}$ and is not available for NAT ~~and STS PSCs~~ PSCs and liquid particles in the mountain wave anymore. Therefore, the largest signal of ~~mountain-wave induced~~ mountain-wave-induced PSCs can be found in ice PSCs in Fig. 11. This is an issue of further investigation in the future. In addition, NAT PSCs are formed by freezing STS particles in the mountain wave, as shown e.g. by Bertram et al. (2000) and Salcedo et al. (2001). This is not integrated in the model so far and should be considered in the future.

The best example of the formation of ~~mountain-wave induced~~ mountain-wave-induced PSCs are ice PSCs (third row in Fig. 11). In the lee of the Antarctic Peninsula ice PSCs occur with volume concentrations as large as $700\,\mathrm{\mu m^3 cm^{-3}}$. These relatively high values might be overestimated ~~since the ice~~ because of the assumptions in the ice scheme of the meteorological model (Doms et al., 2011). As discussed above, the ice number concentration is ~~set to the tropospheric value of which is too large in comparison to measurements, as discussed previously (see also Buchholz, 2005, for an overview).~~ too low for mountain-wave conditions compared to measurements. A more realistic number concentration would lead to smaller ice particles and could reduce the ice volume concentration to more realistic values.

On the other hand, the ice PSCs are clearly connected to the regions where temperature is decreased and show similar wave-like patterns as the temperature. These increased volume concentrations are also present in the global domain where wave-like patterns can be simulated with the nests in contrast to the simulation without the nests where these structures do not exist.

Therefore, this figure shows that ~~mountain-wave induced~~ mountain-wave-induced PSCs can be directly simulated with ICON-ART ~~and their~~ for this specific event. Their effect can also be treated in the global domain where ~~mountain-wave induced~~ mountain-wave-induced PSCs cannot be represented without the nests. The PSCs also interact with the gaseous species which are analysed in the next section.

5.4.2 Influence of the mountain wave on PSC precursors

As mentioned above, long-lived tracers closely follow the potential temperature. Therefore, the wave perturbations in potential temperature can be seen in all tracers shown in Fig. 12 in the lee of the mountain for the simulation with the nests. The wave-like structures in sulfuric acid (H_2SO_4, first row), nitric acid (HNO_3, second row) and water vapour (H_2O, third row) correspond to the structures seen in the potential temperature (see Fig. 5).
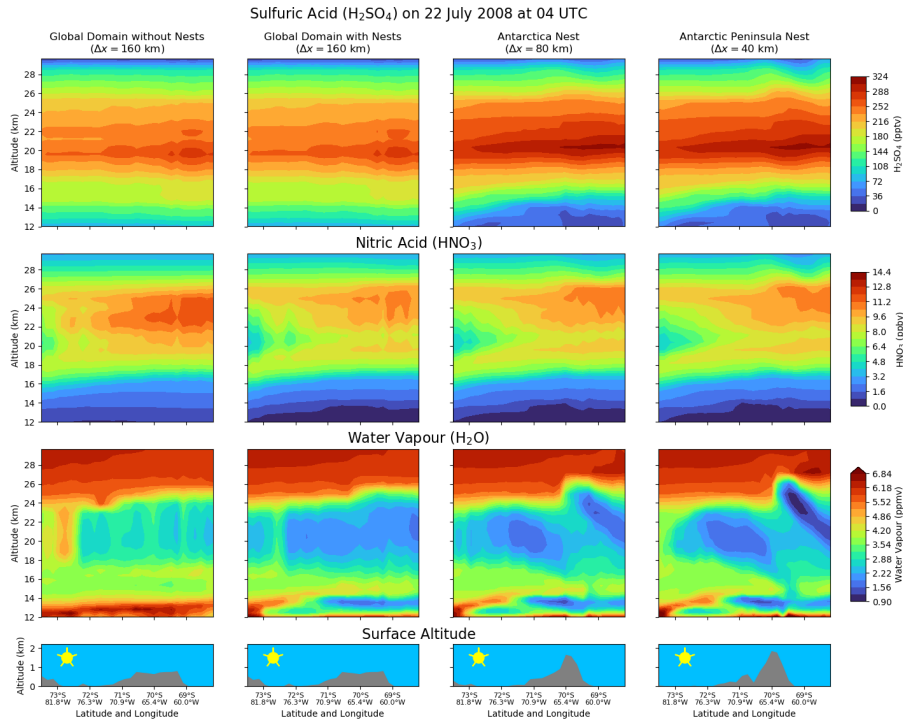
Figure 12. Same as Fig. 5 but for the tracers that are relevant for the formation of PSCs: H_2SO_4, HNO_3 and H_2O. Please note the different colour bars.

~~Sulfuric acid (~~H_2SO_4 ~~) which is prescribed as~~ is prescribed by a climatology in the global domain, but free-running in the nests, and only shows a minor signal of the two-way nesting. Due to the missing sink of H_2SO_4 by sedimentation of aerosols (see Sect. 3) and advection processes, the mixing ratio accumulates in the nested domains (two right columns).

~~Nitric acid (~~HNO_3~~)~~, shown in the second row of Fig. 12, is taken up by STS and NAT PSCs so that it is lower in the simulation with nests than in the simulation without the nests. This is shown not only in ~~the~~ both nested domains, but can also be returned to the global domain as a result of the two-way nesting.

This property especially occurs for ~~water vapour (~~H_2O~~) where in~~. In the lee at altitudes between 22 and 25 km~~with~~, temperatures lower than about 179 K lead to volume mixing ratios lower than 1 ppmv ~~occur~~ that are connected with the uptake in ice PSCs (cf. Fig. 11). The resolution of 80 km in the Antarctica nest (third column) misses a larger part of the wave but the wave-like pattern can still be seen for H_2O. It cannot be represented in the simulation without the nests (left column) where the H_2O volume mixing ratio does not decrease to values lower than 2.5 ppmv. In the global domain of the simulation with the nests, however, values as low as 2 ppmv occur in the lee of the mountain as a result of the two-way nesting.

5.4.3 Impact of ~~mountain-wave induced~~ mountain-wave-induced polar stratospheric clouds on chlorine activation
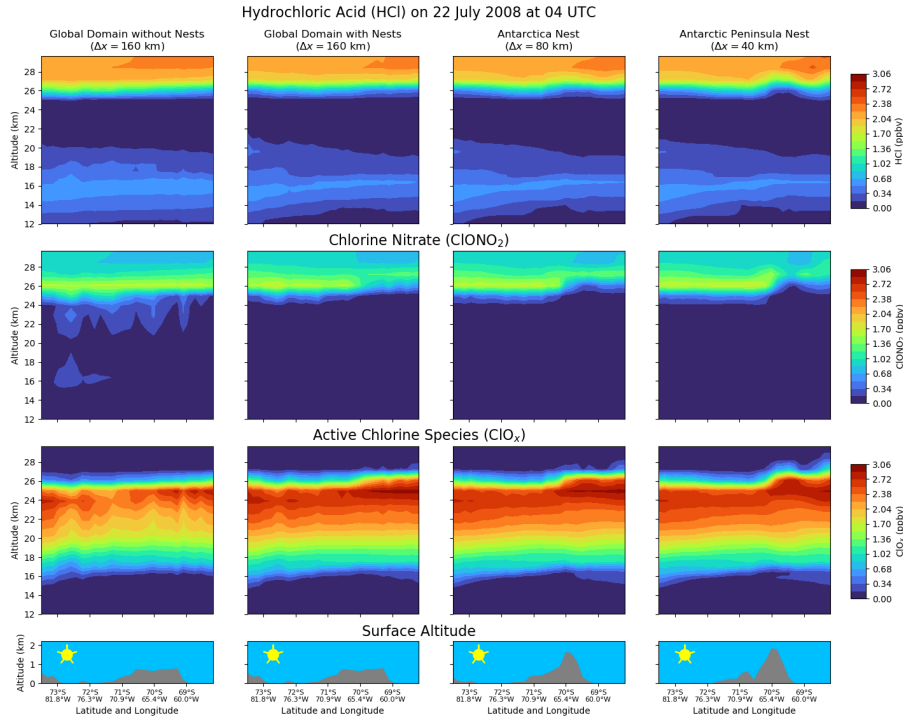
Figure 13. Same as Fig. 5 but for the chlorine species: HCl, ClONO$_2$ and the sum of all other (active) chlorine-containing species (ClO$_x$). The colour bars are equal in this figure.

~~The directly simulated mountain-wave induced PSCs~~ Both the directly simulated mountain-wave-induced PSCs and the lower wave-driven temperature in the simulation with the nests also affect ~~the chemistry due to increased heterogeneous reactions on their surface~~ other species. The chlorine species are summarised in Fig. 13 in the same way as in the previous figures. The reservoir species ~~(~~ hydrochloric acid (HCl, first row) and ~~(~~ chlorine nitrate (ClONO$_2$, second row) are shown together with the active chlorine species (third row), summarised as ClO$_x$:

$$X_{\mathrm{ClO_x}} = X_{\mathrm{ClONO_2}} + 2\,X_{\mathrm{Cl_2O_2}} + X_{\mathrm{OClO}} + 2\,X_{\mathrm{Cl_2}} + X_{\mathrm{BrCl}} + X_{\mathrm{HOCl}} + X_{\mathrm{Cl}} + X_{\mathrm{ClO}} \qquad (3)$$

During July, which is a relatively late stage of the southern polar winter, most of the chlorine species in the altitude range between 15 and 25 km have been already activated (cf., Tully et al., 2011). The broad band of volume mixing ratios of ClO$_x$ with values up to about 2.2 ppbv that are present in all panels of the third row suggests this. Therefore, additional chlorine activation can only be expected in altitude regions above 25 km. In the previous sections, it was shown that the directly simulated ~~mountain-wave induced~~ mountain-wave-induced ice PSCs reaches altitudes of about 26 km (see Fig. 11). ~~Therefore, we focus on these altitudes in the following analyses.~~

~~The mountain-wave induced~~ Low temperature and mountain-wave-induced PSCs lead to increased chlorine activation in the lee of the Antarctic Peninsula that is not present in the simulation without the nests. At altitudes around 26 km, the additional
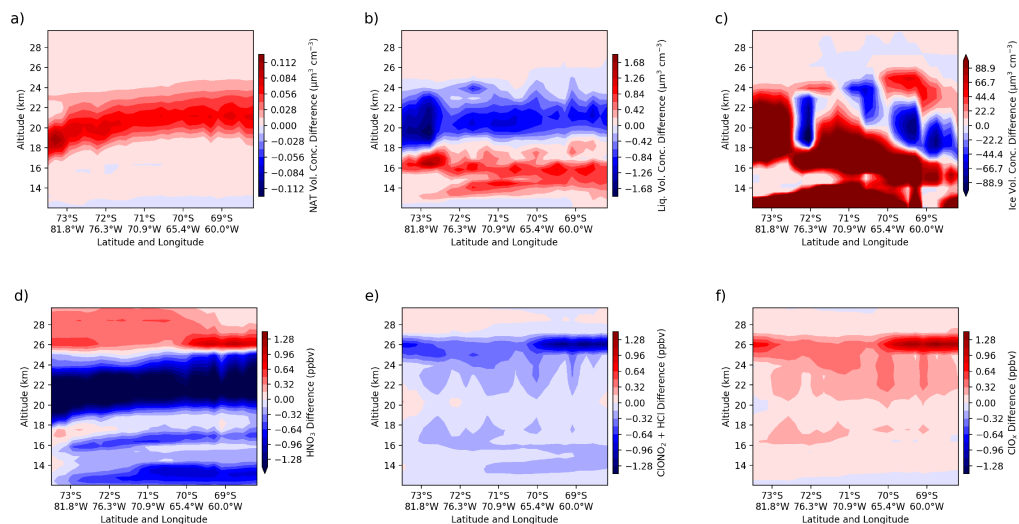
Figure 14. Difference in global domain between with and without nest around the Antarctic Peninsula along the cross section shown in Fig. 2 at the same date (22 July 2008, 04 UTC) and using the same algorithm as in the previous figures. The shown variables are differences in (a-c) the NAT, ~~STS~~ liquid and ice volume concentrations, respectively, (d) the HNO_3 volume mixing ratio, (e) the volume mixing ratio of the reservoir species $ClONO_2$ and HCl and (f) the ClO_x as defined in Eq. (3). Minimum values of HNO_3 are around 2.3 ppbv.

ice PSCs activate both $ClONO_2$ and HCl in the lee of the mountains. This is shown by values of the reservoir species around zero and values of ClO_x up to 3 ppbv in this region that cannot be simulated without the nests. These increased ClO_x mixing ratios also have an effect on ozone in the model which will be shown in the next section.

5.4.4 Impact of mountain-wave-induced polar stratospheric clouds on ozone

665 A summary of the impact of the two-way nesting on ~~mountain-wave induced~~ mountain-wave-induced PSCs and the chemistry can be found in Fig. 14~~where~~. It shows the differences of the two global domains between with and without the nests ~~are shown~~ for various variables of the previous sections. Panel a shows the difference in the NAT volume concentration and it can be seen that more NAT particles are produced in the simulation with the nests as a result of the two-way nesting. These enhanced NAT volume concentrations lead to (1) a decreased volume concentration ~~in STS~~ of liquid particles (panel b) as a result of the used

670 operator splitting and (2) to decreased values of HNO_3 (panel d) with differences lower than -1.4 ppbv in this region since HNO_3 is taken up by NAT particles. In regions where no additional NAT particles exist, the ~~STS~~ liquid volume concentration is enhanced due to the two-way nesting (panel b). In the ice volume concentration in panel c, the wave-like structure is clearly ~~visible~~present.
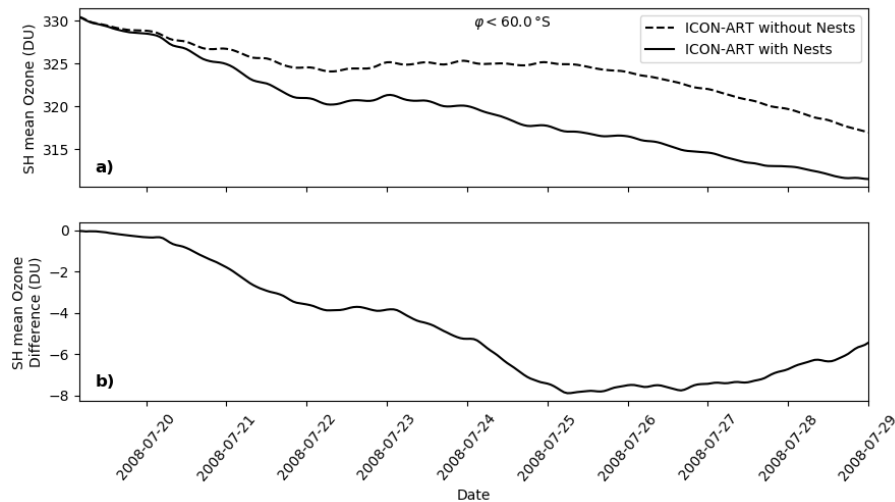
Figure 15. Time series of the mean total ozone column during the third period of the simulation in the global domains for latitudes south of 60 °S (panel a). The dashed line is the simulation without the nests and the solid line shows the ozone development in the simulation with the nests. The difference between these lines is illustrated in panel b.

The ~~mountain-wave induced~~ mountain-wave-induced (ice) PSCs and low temperatures lead to additional chlorine activation, in this example in an altitude of about $26\,\text{km}$ ~~where the~~. The negative difference in the sum of ClONO_2 and HCl (panel e) is closely connected to the positive differences in ClO_x in the lee of the mountain (panel f). HNO_3 is also a product of heterogeneous reactions on the surface of PSCs and therefore is enhanced in this region with respect to the simulation without the nests (panel d).

~~Altogether, it was shown so far that with the local grid refinement around the Antarctic Peninsula mountain-wave induced PSCs can be represented in the global domain where they cannot be simulated without the nests. These PSCs lead to increased chlorine activation in the model.~~

5.4.5 ~~Impact of mountain-wave induced polar stratospheric clouds on ozone~~

Due ~~the mountain wave event in July 2008 above the Antarctic Peninsula, chlorine activation is increased in the simulation with the nests compared to the simulation without the nests. The impact on ozone cannot be expected to be present at the Antarctic Peninsula itself since the~~ to transport of the activated chlorine species ~~are transported during the polar night within the polar vortex~~ and PSCs, ozone depletion might take place downstream of the Antarctic Peninsula (e.g., Höpfner et al., 2006b). Therefore, ozone is affected by the mountain wave event (1) far in the lee of the mountain and (2) later in the year. This is why the time series of the southern hemispheric mean total ozone column for the whole third period of the simulation is shown in Fig. 15. The ozone columns are averaged for latitudes south of 60 °S. Two lines are shown in panel a: the solid line is the mean

total ozone column in the global domain of the simulation with the nests, whereas the dashed line illustrates the simulation without the nests.

As can be seen, differences in the simulations are below 1 DU during the whole day of 19 July (see also panel b). This first day is a spin-up period for the nests that are initialised with the global domain to form the mountain wave. From 20 July until end of the simulation, however, the mean ozone column in the simulation with the nests is smaller than in the simulation without the nests. While ozone is generally decreasing during this period in both simulations, the absolute value of the difference peaks at around 8 DU on 25 July and decreases afterwards. The higher resolution around the Antarctica and the Antarctic Peninsula seems to lead to generally lower ozone columns. This additionally highlights the need of higher resolutions in atmospheric chemistry models.

Figure 15 demonstrates that the higher load of active chlorine species ~~due to the directly and interactively formed mountain-wave induced PSCs lead to~~ leads to a by up to 8 DU larger decrease of ozone in the southern hemisphere. The prediction skill after 10 days is fairly low so that an analysis after the shown period is not possible with a free-running simulation. Future investigations could extend this period with specified dynamics in both simulations to be able to examine the impact of ~~mountain-wave induced~~ mountain-wave-induced PSCs on the ozone hole during September and October.

6 Conclusions and outlook

Seamless modelling of chemistry-climate interactions is challenging. Not many modelling systems can do this in a consistent way. In the past, it was impossible to directly simulate ~~mountain-wave induced polar stratospheric clouds (PSCs)~~ mountain-wave-induced PSCs in global chemistry models due to the coarse resolution in that kind of simulations. In this study, we investigated this problem with the scheme for PSCs in the ICOsahedral Non-hydrostatic modelling framework with its extension for Aerosols and Reactive Trace gases (ICON-ART). The scheme forms ice PSCs based on the microphysics of the meteorological model, ~~STS~~ liquid (sulfate and STS) particles by the analytic expression of Carslaw et al. (1995) with some improvements with respect to the constant particle number concentration and NAT particles by a kinetic non-equilibrium approach with a flexibly selectable size distribution.

We performed a three-step simulation to investigate the impact of ~~mountain-wave induced~~ mountain-wave-induced PSCs in ICON-ART on the chemistry: First, a free-running simulation was conducted from 01 March to 30 April 2008. Second, the dynamics were reinitialised every second day by ERA-Interim data to ensure a realistic development of the polar vortex until 18 July 2008. Third, two free-running simulations followed that covered the investigated mountain wave event from 19 July to 29 July 2008: a simulation including two-way nesting with nests around the Antarctica ($\Delta x \approx 80$ km) and the Antarctic Peninsula ($\Delta x \approx 40$ km) and a simulation without these nests.

The results were compared with measurements by CALIOP and AIRS~~in the Antarctic Peninsula nest. The PSC types~~. The CALIOP PSC categories of ICON-ART were derived from an algorithm that transfers the PSC volume concentrations to the spectral space of CALIOP so that a statistical comparison between both datasets could be established. The ~~CALIOP PSC type "~~total number of grid points with PSCs in ICON-ART was half of that measured by CALIOP although the temperature

distribution was similar. This should be further investigated in future simulations. The CALIOP "Wave-ice"-" category could not be simulated with the model most probably as a result of the constant ice number concentration set to $0.25\,cm^{-3}$. The analyses also showed the need of an interactive calculation of PSCs to treat the different PSC types competing with the available gaseous HNO_3 and H_2O. The comparison with all CALIOP measurements within the Antarctic Peninsula nest demonstrated that the general formation of most of the PSC types PSCs in ICON-ART is similar with respect to temperature. At low temperatures, ice PSCs dominate in both datasets whereas STS and NAT types have the largest fractions for temperatureshigher than the ice formation temperature. This was We found a resolution-dependent overestimation of the fraction of ice clouds in comparison to CALIOP at high temperatures. This suggested that an even higher resolution is needed to capture PSCs in the lowest temperatures. However, the resolution of $40\,km$ clearly improved the PSC formation compared to $160\,km$ and CALIOP. These findings were also pronounced by evaluations with respect to the NAT and ice formation temperatures.

The comparison to AIRS demonstrated for all Antarctic Peninsula overpasses of 20 and 21 July 2008 that the main features of the mountain wave can could be represented in the resolution of $40\,km$. The measured angle of the mountain wave to the mountain range can be represented could be reflected by the model and the brightness temperature perturbation is was in the correct order of magnitude for all overpasses. The investigated mountain wave had a horizontal wavelength of about and is therefore a medium large mountain wave $300\,km$ that could be captured by the chosen resolution. For mountain waves with smaller wavelengths, an even higher resolution would be needed to resolve the wave adequately.

In addition, even though we had chosen a high resolution, compared to standard climate simulations, we still observed structures that could not be resolved. This underlines the need for high-resolution climate simulations for a suitable physical representation of mountain waves.

By introducing the two-way nesting around the Antarctic Peninsula with resolutions down to $40\,km$, we were able to directly simulate the main features of the mountain wave and transfer its effect back to the global domainfor a typical event on 19 to 29 July 2008. . Thus, additional mountain-wave-induced PSCs , formed also in the mountain-wave-induced PSCs together with lower temperatures led to enhanced chlorine activation in the global resolution of $160\,km$, lead to enhanced chlorine activation and with that to an . An up to $8\,DU$ larger ozone depletion above the Antarctic Continent was simulated.

Thus, this demonstrates study shows the need of treating mountain-wave-induced PSCs in CCMs. The study also demonstrated that (1) dynamics, tracers, PSCs and chemistry are interactively and consistently integrated in ICON-ARTand that (2) the . In addition, ICON-ART showed the potential to bridge the gap between direct simulations of mountain-wave induced mountain-wave-induced PSCs and their treatment in coarse global resolutionscan be bridged by ICON-ART.

Future simulations will should exploit the nesting technique further and either use it for other known mountain wave hot spots (e.g., Hoffmann et al., 2013, 2017)or longer periods. In addition, the northern hemisphere will be analysed impact on ozone depletion should be evaluated with measurements and simulations of longer periods. The northern hemisphere should be also a focus in the future where PSC formation and ozone depletion has been shown to be highly sensitive to the existence of mountain waves (e.g., Tabazadeh et al., 2000; Eckermann et al., 2006; Dörnbrack et al., 2012; Khosrawi et al., 2018).

Code and data availability. Licences of the ICON code are currently managed by the Max-Planck-Institute for Meteorology (MPI-M) and the German Weather Service (DWD). Please visit https://code.mpimet.mpg.de/projects/iconpublic/wiki/How_to_obtain_the_model_code (last access on 19 March 2021) for further information. For ART, please contact Bernhard Vogel (bernhard.vogel@kit.edu). The version 2 data of CALIOP PSCs first published in Pitts et al. (2018) can be directly obtained by contacting Michael Pitts (michael.c.pitts@nasa.gov) and will be made available soon at CALIPSO Science Team (2015). The AIRS data is distributed by the NASA Goddard Earth Sciences Data Information and Services Center (AIRS project, 2007). The AIRS gravity wave datasets used in this study can be accessed at https://datapub.fz-juelich.de/slcs/airs/gravity_waves (last access on 19 March 2021). The code to transfer model PSC data to the optical space of CALIOP has been recently published as supplement by Steiner et al. (2021).

Appendix A: ~~Reactions and their rate constants~~ The PSC scheme in ICON-ART

In ~~this appendix, we provide all chemical reactions that are used in this study. Table ?? shows the 93 gasphase reactions. The gasphase reaction rate constants are computed as part of the MECCA module. Table ?? shows the 11 heterogeneous reactions where the reaction rate constants are calculated by the PSC scheme of~~ ICON-ART, the three types of PSCs (ice, NAT and STS) are treated separately. Sensitivity simulations showed that the ICON microphysics for ice clouds, operationally computed up to an altitude of $22.5\,\mathrm{km}$, can be extended to the lower stratosphere up to $30\,\mathrm{km}$ (Weimer, 2019). The hydrometeor microphysics in ICON include heterogeneous nucleation of cloud ice, nucleation of cloud ice due to homogeneous freezing of cloud water and depositional growth and sublimation of cloud ice interacting with the other hydrometeors as well as sedimentation of the ice particles (Doms et al., 2011). Thus, both nucleation of ice PSCs and dehydration of the lower stratosphere can be captured by the ICON microphysics. A similar approach is used in the Whole Atmosphere Community Climate Model (WACCM, Wegner et al., 2013). Ice particle radius (r_{ice} in m) and particle number concentration (N_{ice} in m^{-3}) correspond to the assumed size distributions in the microphysics (Doms et al., 2011):

$$N_{\mathrm{ice}}(T) = \min\left(5\exp\left[0.304\left(273.15 - T\right)\right], 250\times 10^3\right)$$

$$r_{\mathrm{ice}} = \frac{1}{2}$$

$$\left]\frac{\rho\, q_{\mathrm{ice}}}{130\, N_{\mathrm{ice}}}\right.$$

where ρ is the air density in $\mathrm{kg\,m^{-3}}$, T is the temperature in K and q_{ice} is the mass mixing ratio in $\mathrm{kg\,kg^{-1}}$ of water in ice. Equation A1 means that the ice particle number concentration is assumed to be $0.25\,\mathrm{cm^{-3}}$ for temperatures lower than $239\,\mathrm{K}$.

Two parametrisations for the microphysics of NAT particles are integrated in ICON-ART. ~~Finally, the 38 photolytic reactions are summarised in Table ??. Photolysis rates are calculated by the CloudJ module (Prather, 2015).~~ The thermodynamic NAT parametrisation is diagnostic and therefore computes the number of moles of NAT particles in thermodynamic equilibrium, calculates its sedimentation and evaporates the particles again within the same model time step. The volume mixing ratio of HNO_3 condensed in NAT ($X_{\mathrm{HNO_3(NAT)}}$ in $\mathrm{mol\,mol^{-1}}$) is calculated on the basis of the difference between vapour pressure of

HNO$_3$ ($p_{\mathrm{HNO_3}}$ in Pa) and the saturation vapour pressure over NAT ($p_{\mathrm{sat,NAT}}$ in Pa):

$$X_{\mathrm{HNO_3(NAT)}} = \frac{p_{\mathrm{HNO_3}} - p_{\mathrm{sat,NAT}}}{p} \tag{A2}$$

Gasphase reactions. The reaction rates constants in the second column are given in units of either or depending on the type of the reaction. Reaction rate constants are provided by the MECCA module, incorporated in ICON-ART. Reaction Rate Constant (cgs-system) 3.3E-11*EXP(55./temp) + + → + 6.E-34*((temp/300.)**(-2.4))*cair + → 2 1.2E-10 + → 2 8.E-12*EXP(-2060./temp) + + → + k_3rd(temp,cair,4.4E-32,1.3,7.5E-11,-0.2,0.6) + → + 1.4E-10*EXP(-470./temp) + → +1.2E-10 + → +1.8E-11*EXP(180./temp) + → +1.7E-12*EXP(-940./temp) + → + 2.8E-12*EXP(-1800./temp) + → + 3.E-11*EXP(200./temp) + → 2 1.E-14*EXP(-490./temp) + → 2 7.2E-11 + → + 6.9E-12 + → +1.6E-12 + → + 4.8E-11*EXP(250./temp) + + → + + k_HO2_HO2 + → 2 1.63E-10*EXP(60./temp) + → +1.8E-12 + → +1.5E-11*EXP(-3600./temp) + → +2.15E-11*EXP(110./temp) + → 2 7.25E-11*EXP(20./temp) + → + 4.63E-11*EXP(20./temp) + → + 3.E-12*EXP(-1500./temp) + → + 2.1E-11*EXP(100./temp) The saturation vapour pressure over NAT is calculated according to Hanson and Mauersberger (1988) and p is the air pressure (in Pa). Particle number concentration (N_{NAT}) and radius (r_{NAT}) in the thermodynamic NAT parametrisation are calculated using a threshold in the number concentration of $N_{\mathrm{NAT,max}} = 2.3 \times 10^{-4}\,\mathrm{cm^{-3}}$ which is based on van den Broek et al. (2004). Below this threshold, the radius of the NAT particles is set to $0.1\,\mu\mathrm{m}$. Above this threshold, the particle number concentration is set to $N_{\mathrm{NAT,max}}$ and the radius of the particles is increased accordingly. This method has already been used in a similar way for solid particles by Kirner et al. (2011).

Continued. Reaction Rate Constant (cgs-system) + → + 5.1E-12*EXP(210./temp) + → +1.2E-13*EXP(-2450./temp) + → + 5.8E-12*EXP(220./temp) + → 2 1.5E-11*EXP(170./temp) + + → + k_NO3_NO2 + → + + k_NO3_NO2/(2.7E-27 + → + 3.3E-12*EXP(270./temp) + + → The kinetic NAT parametrisation is a non-equilibrium approach based on prognostic equations for the particle mass (see e.g., Seinfeld and Pandis, 2006, p. 539). Carslaw et al. (2002) applied this approach to NAT particles in a Lagrangian model and van den Broek et al. (2004) extended it to Eulerian models. In the Lagrangian description by Carslaw et al. (2002), the change in NAT particle radius ($r_{\mathrm{NAT},b}$) is calculated prognostically by a diffusive growth

$$\frac{\mathrm{d}r_{\mathrm{NAT},b}}{\mathrm{d}t} = \frac{G_b}{r_{\mathrm{NAT},b}} \tag{A3}$$

where G_b (in $\mathrm{m^2\,s^{-1}}$) is a growth factor which depends on the diffusion coefficient of HNO$_3$ in air ($D_{\mathrm{HNO_3}}$, in $\mathrm{m^2\,s^{-1}}$), the air temperature (T, in K) and the saturation difference of the HNO$_3$ + k_3rd(temp,cair,1.8E-30,3.0,2.8E-11,0.,0.6) + + → + k_NO2_HO2 + → + k_HNO3_OH + → + + k_NO2_HO2/(2.1E-27*EXP(10900./temp)) + → +1.3E-12*EXP(380./ + → .75 + .75 + .25 + .4 + .05 + → +1.85E-20*EXP(2.82*log(temp)-987./temp) + → + 4.1E-13*EXP(750./temp) + → + + 2.8E-12*EXP(300./temp) 2.*RO2*9.5E-14*EXP(390./temp)/(1.+1./26.2*EXP(1130./temp)) → .5 + .5 + .5 2.*RO2*9.5E-14*EXP(390./temp)/(1.+26.2*EXP(-1130./temp)) + → .7 + .3 + .3 + + → + + 9.52E-18*EXP(2.03*log(temp)+636./temp) + → + (1.57E-13+cair*3.54E-33) + → +2.8E-11*EXP(-250./te

vapour pressure (in Pa):

$$G_b = \frac{D^*_{\mathrm{HNO_3},b} M_{\mathrm{NAT}}}{\rho_{\mathrm{NAT}} R^* T} \left(p_{\mathrm{HNO_3}} - p_{\mathrm{sat,NAT}} \right) \tag{A4}$$

with

$$D^*_{\mathrm{HNO_3},b} = \frac{D_{\mathrm{HNO_3}}}{1 + 4 D_{\mathrm{HNO_3}}/(\overline{v}_{\mathrm{HNO_3}} r_{\mathrm{NAT},b})} \tag{A5}$$

In these equations, $\overline{v}_{\mathrm{HNO_3}}$ is the mean thermal velocity of air molecules (in $\mathrm{m\,s^{-1}}$), R^* stands for the universal constant of an ideal gas in $\mathrm{J\,mol^{-1}\,K^{-1}}$, ρ_{NAT} is the crystal density of NAT ($1.626 \times 10^6\,\mathrm{g\,m^{-3}}$, Drdla et al., 1993; and M_{NAT} is the NAT molar mass of $117\,\mathrm{g\,mol^{-1}}$. In one of the Eulerian formulations by van den Broek et al. (2004), this radius change is applied to particles in size bins, but directly converted into a change in the particle number concentration ("FixedRad" approach). This approach is used in this study with a size distribution based on van den Broek et al. (2004) as shown in Fig. 3. That is why we added a b subscript to all variables in Eqs. (A3), (A4) and (A5) that depend on the size bin b.

The size distribution of NAT particles can be flexibly specified by the user to investigate its impact on denitrification without any change in the Fortran code but rather changing the respective XML control file (cf. Schröter et al., 2018). Each size bin is defined by radius limits and a maximum particle number concentration, which are kept constant during the simulation. If the calculated particle number concentration in a bin exceeds the maximum, the excess mass is transferred to the next larger size bin. The sum of the maximum particle number concentrations of the bins has to equal the value by van den Broek et al. (2004), which is $2.3 \times 10^{-4}\,\mathrm{cm^{-3}}$ and based on measurements of large NAT particles. Sensitivity studies by van den Broek et al. (2004) showed that this value in combination with the used size distribution leads to denitrification comparable to measurements. The size bins are transported as passive tracers in ICON-ART.

 Since the calculation of $p_{\mathrm{sat,NAT}}$ by Hanson and Mauersberger (1988) has specific temperature limits, NAT particles are evaporated automatically at temperatures higher than $220\,\mathrm{K}$. For temperatures below $180\,\mathrm{K}$, we calculate $p_{\mathrm{HNO_3}}$ with a constant temperature of $180\,\mathrm{K}$. These two NAT parametrisations are also implemented in the ECHAM/MESSy Atmospheric Chemistry model (EMAC, Jöckel et al., 2010; Kirner et al., 2011).

~~+ + → + k_BrO_NO2 + → + + 7.7E-12*EXP(-580./temp) + → + 2.35E-12*EXP(-1300./temp) + → +~~
~~1.6E-12*EXP(430./temp) + → + + 2.9E-12*EXP(220./temp) + → + 5.8E-13*EXP(170./temp) + → +~~
~~k_3rd(temp,cair,3.3E-31,4.3,1.6E-12,0.,0.6)~~ Sedimentation of NAT particles, either formed by thermodynamic
or kinetic NAT parametrisation, is calculated by a simple upwind method, using the Stokes velocity of assumed spherical
particles (Stokes, 1851).

The microphysics of liquid (sulfate and STS) particles in the module are calculated by the scheme first published by
Carslaw et al. (1995), with one exception: in the original code by Carslaw et al. (1995) the particle number concentration is set
to the constant value of $10\,\mathrm{cm}^{-3}$. We improved this fixed value by applying the mean of all balloon-borne STS measurements
by Hervig and Deshler (1998) in order to derive the particle surface area concentration S_{STS} and the radius r_{STS} of STS
particles from the internally calculated particle volume concentration V_{STS}:

$$S_{\mathrm{STS}} = 6.068\,(V_{\mathrm{STS}})^{0.671} \tag{A6}$$

$$r_{\mathrm{STS}} = \frac{3\,V_{\mathrm{STS}}}{S_{\mathrm{STS}}} \tag{A7}$$

~~Heterogeneous reactions. Reaction rate constants are calculated by the PSC scheme of ICON-ART. The uptake coefficients~~
~~of the different PSC types are taken from Sander et al. (2011b), where not stated differently. Reaction γ_{STS} γ_{NAT} γ_{ice}~~ In these
equations, V_{STS} has to be given in $\mu\mathrm{m}^3\mathrm{cm}^{-3}$ to get S_{STS} and r_{STS} in $\mu\mathrm{m}^2\mathrm{cm}^{-3}$ and $\mu\mathrm{m}$, respectively. Sedimentation is
neglected for liquid particles since they are too small to result in relevant redistribution of the major constituents H_2O, HNO_3
and H_2SO_4 (Tabazadeh et al., 2000; Considine et al., 2000).

Since the PSCs in the current version of the model do not interact with each other like in a fully coupled PSC scheme
(e.g., Zhu et al., 2015), there are essentially two approaches to calculate PSCs: either they are computed with the total (gaseous
+ ~~→ 2 (a) 0.0004 0.027~~ liquid + ~~→ + (a) 0.1 0.2 + → +~~ solid) concentrations of HNO_3 ~~(a) 0.2 0.3 +~~ and H_2O ~~→ +~~ as input
for all PSC types (e.g., Kirner et al., 2011) or the PSCs are calculated subsequently with the gaseous fraction that remains after
formation of the previously calculated PSC types (operator splitting). Both approaches have their advantages and disadvantages.
We use the second approach because the maximum of HNO_3 ~~(a) 0.004 0.3 + → + (a) 0.003 0.03 + → +~~ and H_2O ~~(a) 0.1[b]~~
~~0.1 + → + (a) 0.001[b] 0.26 + → + (a) 0.3 0.3 + → + (a) 0.3[b] 0.26 + → + (a) 0.3[b] 0.3[c] + → + (a) 0.1[b] 0.3~~

taken up by PSCs cannot exceed the gaseous concentrations in this case. First, ice PSCs are calculated, then NAT PSCs and
finally liquid particles.

Particle radius, particle number concentration and particle surface area concentration are used to calculate the heterogeneous
reaction rate constants on the surface of PSCs. For NAT and ice, which can grow to relatively large sizes in the order of
tens of $\mu\mathrm{m}$, the following equation is used to calculate the heterogeneous reaction rate constant, assuming spherical particles
(Drdla et al., 1993):

$$k_{\mathrm{het},h,c} = \frac{\gamma_{h,c}\,\pi r_c^2\,\overline{v}_{i(h)}\,N_c}{N_{j(h)}\left(1 + \frac{3\gamma_{h,c}}{4\mathrm{Kn}}\right)}, \quad c \in \{\mathrm{NAT, ice}\} \tag{A8}$$

where $\gamma_{h,c}$ is the uptake coefficient (i.e. reaction probability) of heterogeneous reaction h and PSC type c, $\overline{v}_{i(h)}$ is the mean thermal velocity of the gaseous reactant $i(h)$ (in $\mathrm{m\,s^{-1}}$), N_c is the PSC number concentration and $N_{j(h)}$ is the number concentration of the reactant $j(h)$ adsorbed on the particle (both in $\mathrm{m^{-3}}$). The Knudsen number Kn is calculated by $\lambda_{\mathrm{mfp}}/r_c$ with the mean free path λ_{mfp} of air molecules (in m), calculated according to Kennard (1938). In case of the kinetic NAT parametrisation, Eq. (A8) is evaluated for each size bin separately and summed up subsequently.

Photolytic reactions. Photolysis rates are calculated by the CloudJ module, incorporated in ICON-ART. Reaction $+ \rightarrow + +$ $\rightarrow + + \rightarrow + + \rightarrow + + \rightarrow 2 + \rightarrow + + \rightarrow + + \rightarrow + + \rightarrow + + \rightarrow + + \rightarrow + + \rightarrow .667 + .667 + .333 + .333 + \rightarrow + + + \rightarrow + +$ $\rightarrow + + + \rightarrow + + \rightarrow + 0.31 + 0.69 + 1.155 + \rightarrow + + \rightarrow 2 + \rightarrow + + \rightarrow + + \rightarrow + + \rightarrow + + \rightarrow + + \rightarrow + + \rightarrow 4 + \rightarrow 3 + \rightarrow 3 + \rightarrow$ $2 + \rightarrow + + \rightarrow +$ Liquid particles are considerably smaller than ice and NAT particles (e.g., Considine et al., 2000) and hence $\mathrm{Kn} \gg 1$ so that the slip flow correction term in Eq. (A8) can be neglected, which yields:

$$k_{\mathrm{het},h,\mathrm{liq}} = \frac{\gamma_{h,\mathrm{liq}}\overline{v}_{i(h)}S_{\mathrm{liq}}}{4N_{j(h)}} \tag{A9}$$

Continued. Reaction$+ \rightarrow + + \rightarrow 0.85 + 0.85 + 0.15 + 0.15 + \rightarrow + + \rightarrow + \rightarrow + + \rightarrow +$ The total reaction rate constant is the sum of the reaction rate constants on all three types of PSCs. The uptake coefficients in ICON-ART are used either from Carslaw et al. (1995) or Sander et al. (2011b). A summary of the γ values can be found in Table S3 of the paper's supplement. They also compare well to other models (e.g., Solomon et al., 2015).

Author contributions. This paper is part of MW's thesis supervised by PB, RR and OK. MW developed the module for PSCs in ICON-ART and performed the simulations with contributions by JB, OK, RR and PB. LH performed the comparison between AIRS and ICON-ART. MW, BL, IT and MS performed the comparison between ICON-ART and CALIOP. MW prepared the manuscript with contributions by all authors.

Competing interests. The authors declare that they have no conflict of interest.

Acknowledgements. Parts of the simulations were performed on bwUniCluster for which the authors acknowledge support by the state of Baden-Württemberg through bwHPC. Other parts of the work as well as evaluations were performed on the supercomputer ForHLR funded by the Ministry of Science, Research and the Arts Baden-Württemberg and by the Federal Ministry of Education and Research. This work was performed with the help of the Large Scale Data Facility at the Karlsruhe Institute of Technology funded by the Ministry of Science, Research and the Arts Baden-Württemberg and by the Federal Ministry of Education and Research. We acknowledge ECCAD for archiving and distributing the emission data. We acknowledge funding from the Initiative and Networking Fund of the Helmholtz Association through the projects "Digital Earth" and "Advanced Earth System Modelling Capacity". I. Tritscher was funded by the Deutsche Forschungsgemeinschaft (DFG) under project number 310479827.

References

AIRS project: AIRS/Aqua L1B Infrared (IR) geolocated and calibrated radiances V005, https://doi.org/10.5067/YZEXEVN4JGGJ, Greenbelt, MD, USA, Goddard Earth Sciences Data and Information Services Center (GES DISC), Accessed: 31 December 2015, 2007.

Alexander, M. J. and Teitelbaum, H.: Observation and analysis of a large amplitude mountain wave event over the Antarctic peninsula, Journal of Geophysical Research: Atmospheres, 112, https://doi.org/10.1029/2006JD008368, 2007.

Alexander, S. P., Klekociuk, A. R., Pitts, M. C., McDonald, A. J., and Arevalo-Torres, A.: The effect of orographic gravity waves on Antarctic polar stratospheric cloud occurrence and composition, J. Geophys. Res.: Atmos., 116, https://doi.org/10.1029/2010JD015184, 2011.

Alexander, S. P., Klekociuk, A. R., McDonald, A. J., and Pitts, M. C.: Quantifying the role of orographic gravity waves on polar stratospheric cloud occurrence in the Antarctic and the Arctic, J. Geophys. Res.: Atmos., 118, 11,493–11,507, https://doi.org/10.1002/2013JD020122, 2013.

Aumann, H. H., Chahine, M. T., Gautier, C., Goldberg, M. D., Kalnay, E., McMillin, L. M., Revercomb, H., Rosenkranz, P. W., Smith, W. L., Staelin, D. H., Strow, L. L., and Susskind, J.: AIRS/AMSU/HSB on the Aqua mission: design, science objectives, data products, and processing systems, IEEE Trans. Geosci. Remote Sens., 41, 253–264, https://doi.org/10.1109/TGRS.2002.808356, 2003.

Bacmeister, J.: Mountain-Wave Drag in the Stratosphere and Mesosphere Inferred from Observed Winds and a Simple Mountain-Wave Parameterization Scheme, J. Atmos. Sci., 50, 377–399, https://doi.org/10.1175/1520-0469(1993)050<0377:MWDITS>2.0.CO;2, 1993.

Bacmeister, J. T., Newman, P. A., Gary, B. L., and Chan, K. R.: An Algorithm for Forecasting Mountain Wave-Related Turbulence in the Stratosphere, Weather Forecast., 9, 241–253, https://doi.org/10.1175/1520-0434(1994)009<0241:AAFFMW>2.0.CO;2, 1994.

Bertram, A. K., Dickens, D. B., and Sloan, J. J.: Supercooling of type 1 polar stratospheric clouds: The freezing of submicron nitric acid aerosols having HNO_3 mol fractions less than 0.5, J. Geophys. Res.: Atmos., 105, 9283–9290, https://doi.org/10.1029/1999JD901174, 2000.

Braesicke, P., J. Neu (Lead Authors), Fioletov, V., Godin-Beekmann, S., Hubert, D., Petropavlovskikh, I., Shiotani, M., and Sinnhuber, B.-M.: Chapter 3: Update on Global Ozone: Past, Present, and Future, in: Scientific Assessment of Ozone Depletion: 2018, edited by Fahey, D. W., Newman, P. A., Pyle, J. A., and Safari, B., Global Ozone Research and Monitoring Project – Report No. 58, World Meteorological Organization, Geneva, Switzerland, 2018.

Buchholz, J.: Simulations of Physics and Chemistry of Polar Stratospheric Clouds with a General Circulation Model, Ph.D. thesis, Johannes-Gutenberg University, Mainz, Germany, 2005.

CALIPSO Science Team: CALIPSO Lidar Level 2 Polar Stratospheric Clouds (PSC) Data Product Ensemble, Provisional V1-10, https://doi.org/10.5067/CALIOP/CALIPSO/CAL_LID_L2_PSCMASK-PROV-V1-00_L2-001.00, 2015.

Carslaw, K. S., Luo, B. P., Clegg, S. L., Peter, T., Brimblecombe, P., and Crutzen, P. J.: Stratospheric aerosol growth and HNO_3 gas phase depletion from coupled HNO_3 and water uptake by liquid particles, Geophys. Res. Lett., 21, 2479–2482, https://doi.org/10.1029/94GL02799, 1994.

Carslaw, K. S., Luo, B., and Peter, T.: An analytic expression for the composition of aqueous HNO_3-H_2SO_4 stratospheric aerosols including gas phase removal of HNO_3, Geophys. Res. Lett., 22, 1877–1880, https://doi.org/10.1029/95GL01668, 1995.

Carslaw, K. S., Wirth, M., Tsias, A., Luo, B. P., Dörnbrack, A., Leutbecher, M., Volkert, H., Renger, W., Bacmeister, J. T., and Peter, T.: Particle microphysics and chemistry in remotely observed mountain polar stratospheric clouds, J. Geophys. Res.: Atmos., 103, 5785–5796, https://doi.org/10.1029/97JD03626, 1998a.

Carslaw, K. S., Wirth, M., Tsias, A., Luo, B. P., Dörnbrack, A., Leutbecher, M., Volkert, H., Renger, W., Bacmeister, J. T., Reimer, E., and Peter, T.: Increased stratospheric ozone depletion due to mountain-induced atmospheric waves, Nature, 391, 675–678, https://doi.org/10.1038/35589, https://doi.org/10.1038/35589, 1998b.

950 Carslaw, K. S., Peter, T., Bacmeister, J. T., and Eckermann, S. D.: Widespread solid particle formation by mountain waves in the Arctic stratosphere, Journal of Geophysical Research: Atmospheres, 104, 1827–1836, https://doi.org/https://doi.org/10.1029/1998JD100033, https://agupubs.onlinelibrary.wiley.com/doi/abs/10.1029/1998JD100033, 1999.

Carslaw, K. S., Kettleborough, J. A., Northway, M. J., Davies, S., Gao, R.-S., Fahey, D. W., Baumgardner, D. G., Chipperfield, M. P., and Kleinböhl, A.: A vortex-scale simulation of the growth and sedimentation of large nitric acid hydrate particles, J. Geophys. Res.: Atmos.,
955 107, SOL 43–1–SOL 43–16, https://doi.org/10.1029/2001JD000467, 8300, 2002.

Chahine, M. T., Pagano, T. S., Aumann, H. H., Atlas, R., Barnet, C., Blaisdell, J., Chen, L., Divakarla, M., Fetzer, E. J., Goldberg, M., Gautier, C., Granger, S., Hannon, S., Irion, F. W., Kakar, R., Kalnay, E., Lambrigtsen, B. H., Lee, S.-Y., Le Marshall, J., Mcmillan, W. W., McMillin, L., Olsen, E. T., Revercomb, H., Rosenkranz, P., Smith, W. L., Staelin, D., Strow, L. L., Susskind, J., Tobin, D., Wolf, W., and Zhou, L.: AIRS: Improving Weather Forecasting and Providing New Data on Greenhouse Gases, B. Am. Meteorol. Soc., 87, 911–926,
960 https://doi.org/10.1175/BAMS-87-7-911, 2006.

Considine, D. B., Douglass, A. R., Connell, P. S., Kinnison, D. E., and Rotman, D. A.: A polar stratospheric cloud parameterization for the global modeling initiative three-dimensional model and its response to stratospheric aircraft, J. Geophys. Res.: Atmos., 105, 3955–3973, https://doi.org/10.1029/1999JD900932, 2000.

Cunnold, D. M., Fraser, P. J., Weiss, R. F., Prinn, R. G., Simmonds, P. G., Miller, B. R., Alyea, F. N., and Crawford, A. J.: Global trends
965 and annual releases of CCl_3F and CCl_2F_2 estimated from ALE/GAGE and other measurements from July 1978 to June 1991, J. Geophys. Res.: Atmos., 99, 1107–1126, https://doi.org/10.1029/93JD02715, 1994.

Dee, D. P., Uppala, S. M., Simmons, A. J., Berrisford, P., Poli, P., Kobayashi, S., Andrae, U., Balmaseda, M. A., Balsamo, G., Bauer, P., Bechtold, P., Beljaars, A. C. M., van de Berg, L., Bidlot, J., Bormann, N., Delsol, C., Dragani, R., Fuentes, M., Geer, A. J., Haimberger, L., Healy, S. B., Hersbach, H., Hólm, E. V., Isaksen, L., Kållberg, P., Köhler, M., Matricardi, M., McNally, A. P., Monge-Sanz, B. M., Mor-
970 crette, J.-J., Park, B.-K., Peubey, C., de Rosnay, P., Tavolato, C., Thépaut, J.-N., and Vitart, F.: The ERA-Interim reanalysis: configuration and performance of the data assimilation system, Q. J. Roy. Meteor. Soc., 137, 553–597, https://doi.org/10.1002/qj.828, 2011.

Diehl, T., Heil, A., Chin, M., Pan, X., Streets, D., Schultz, M., and Kinne, S.: Anthropogenic, biomass burning, and volcanic emissions of black carbon, organic carbon, and SO_2 from 1980 to 2010 for hindcast model experiments, Atmos. Chem. Phys. Discuss., 12, 24 895–24 954, https://doi.org/10.5194/acpd-12-24895-2012, 2012.

975 Dipankar, A., Stevens, B., Heinze, R., Moseley, C., Zängl, G., Giorgetta, M., and Brdar, S.: Large eddy simulation using the general circulation model ICON, J. Adv. Model. Earth Sy., 7, 963–986, https://doi.org/10.1002/2015MS000431, 2015.

Doms, G., Förstner, J., Heise, E., Herzog, H.-J., Mironov, D., Raschendorfer, M., Reinhardt, T., Ritter, B., Schrodin, R., Schulz, J.-P., and Vogel, G.: A Description of the Nonhydrostatic Regional COSMO Model. Part II: Physical Parametrization, Tech. rep., Deutscher Wetterdienst, Offenbach, 2011.

980 Dörnbrack, A., Birner, T., Fix, A., Flentje, H., Meister, A., Schmid, H., Browell, E. V., and Mahoney, M. J.: Evidence for inertia gravity waves forming polar stratospheric clouds over Scandinavia, J. Geophys. Res.: Atmospheres, 107, SOL 30–1–SOL 30–18, https://doi.org/https://doi.org/10.1029/2001JD000452, https://agupubs.onlinelibrary.wiley.com/doi/abs/10.1029/2001JD000452, 2002.

Dörnbrack, A., Pitts, M. C., Poole, L. R., Orsolini, Y. J., Nishii, K., and Nakamura, H.: The 2009–2010 Arctic stratospheric winter – general evolution, mountain waves and predictability of an operational weather forecast model, Atmos. Chem. Phys., 12, 3659–3675, https://doi.org/10.5194/acp-12-3659-2012, 2012.

Dörnbrack, A., Kaifler, B., Kaifler, N., Rapp, M., Wildmann, N., Garhammer, M., Ohlmann, K., Payne, J. M., Sandercock, M., and Austin, E. J.: Unusual appearance of mother-of-pearl clouds above El Calafate, Argentina (50°21′S, 72°16′W), Weather, 75, 378–388, https://doi.org/https://doi.org/10.1002/wea.3863, https://rmets.onlinelibrary.wiley.com/doi/abs/10.1002/wea.3863, 2020.

Drdla, K., Turco, R. P., and Elliott, S.: Heterogeneous chemistry on Antarctic polar stratospheric clouds: A microphysical estimate of the extent of chemical processing, J. Geophys. Res.: Atmos., 98, 8965–8981, https://doi.org/10.1029/93JD00164, 1993.

Eckermann, S. D., Dörnbrack, A., Flentje, H., Vosper, S. B., Mahoney, M. J., Bui, T. P., and Carslaw, K. S.: Mountain Wave-Induced Polar Stratospheric Cloud Forecasts for Aircraft Science Flights during SOLVE/THESEO 2000, Weather Forecast., 21, 42–68, https://doi.org/10.1175/WAF901.1, 2006.

Eckermann, S. D., Hoffmann, L., Höpfner, M., Wu, D. L., and Alexander, M. J.: Antarctic NAT PSC belt of June 2003: Observational validation of the mountain wave seeding hypothesis, Geophys. Res. Lett., 36, https://doi.org/10.1029/2008GL036629, 2009.

Engel, I., Luo, B. P., Pitts, M. C., Poole, L. R., Hoyle, C. R., Grooß, J.-U., Dörnbrack, A., and Peter, T.: Heterogeneous formation of polar stratospheric clouds – Part 2: Nucleation of ice on synoptic scales, Atmos. Chem. Phys., 13, 10 769–10 785, https://doi.org/10.5194/acp-13-10769-2013, 2013.

Engel, I., Luo, B. P., Khaykin, S. M., Wienhold, F. G., Vömel, H., Kivi, R., Hoyle, C. R., Grooß, J.-U., Pitts, M. C., and Peter, T.: Arctic stratospheric dehydration – Part 2: Microphysical modeling, Atmos. Chem. Phys., 14, 3231–3246, https://doi.org/10.5194/acp-14-3231-2014, 2014.

Fahey, D. W., Gao, R. S., Carslaw, K. S., Kettleborough, J., Popp, P. J., Northway, M. J., Holecek, J. C., Ciciora, S. C., McLaughlin, R. J., Thompson, T. L., Winkler, R. H., Baumgardner, D. G., Gandrud, B., Wennberg, P. O., Dhaniyala, S., McKinney, K., Peter, T., Salawitch, R. J., Bui, T. P., Elkins, J. W., Webster, C. R., Atlas, E. L., Jost, H., Wilson, J. C., Herman, R. L., Kleinböhl, A., and von König, M.: The Detection of Large HNO_3-Containing Particles in the Winter Arctic Stratosphere, Science, 291, 1026–1031, https://doi.org/10.1126/science.1057265, 2001.

Fritts, D. C. and Alexander, M. J.: Gravity wave dynamics and effects in the middle atmosphere, Rev. Geophys., 41, https://doi.org/10.1029/2001RG000106, 2003.

Fueglistaler, S., Buss, S., Luo, B. P., Wernli, H., Flentje, H., Hostetler, C. A., Poole, L. R., Carslaw, K. S., and Peter, T.: Detailed modeling of mountain wave PSCs, Atmos. Chem. Phys., 3, 697–712, https://doi.org/10.5194/acp-3-697-2003, 2003.

Gelaro, R., McCarty, W., Suárez, M. J., Todling, R., Molod, A., Takacs, L., Randles, C. A., Darmenov, A., Bosilovich, M. G., Reichle, R., Wargan, K., Coy, L., Cullather, R., Draper, C., Akella, S., Buchard, V., Conaty, A., da Silva, A. M., Gu, W., Kim, G.-K., Koster, R., Lucchesi, R., Merkova, D., Nielsen, J. E., Partyka, G., Pawson, S., Putman, W., Rienecker, M., Schubert, S. D., Sienkiewicz, M., and Zhao, B.: The Modern-Era Retrospective Analysis for Research and Applications, Version 2 (MERRA-2), J. Climate, 30, 5419–5454, https://doi.org/10.1175/JCLI-D-16-0758.1, 2017.

Geller, M. A., Alexander, M. J., Love, P. T., Bacmeister, J., Ern, M., Hertzog, A., Manzini, E., Preusse, P., Sato, K., Scaife, A. A., and Zhou, T.: A Comparison between Gravity Wave Momentum Fluxes in Observations and Climate Models, J. Climate, 26, 6383 – 6405, https://doi.org/10.1175/JCLI-D-12-00545.1, https://journals.ametsoc.org/view/journals/clim/26/17/jcli-d-12-00545.1.xml, 2013.

Giorgetta, M. A., Brokopf, R., Crueger, T., Esch, M., Fiedler, S., Helmert, J., Hohenegger, C., Kornblueh, L., Köhler, M., Manzini, E., Mauritsen, T., Nam, C., Raddatz, T., Rast, S., Reinert, D., Sakradzija, M., Schmidt, H., Schneck, R., Schnur, R., Silvers, L., Wan, H.,

Zängl, G., and Stevens, B.: ICON-A, the Atmosphere Component of the ICON Earth System Model: I. Model Description, J. Adv. Model. Earth Sy., 18, https://doi.org/10.1029/2017MS001242, 2018.

Granier, C., Bessagnet, B., Bond, T., D'Angiola, A., Denier van der Gon, H., Frost, G., Heil, A., Kaiser, J., Kinne, S., Klimont, Z., Kloster, S., Lamarque, J.-F., Liousse, C., Masui, T., Meleux, F., Mieville, A., Ohara, T., Raut, J.-C., Riahi, K., Schultz, M., Smith, S., Thompson, A., van Aardenne, J., van der Werf, G., and van Vuuren, D.: Evolution of anthropogenic and biomass burning emissions of air pollutants at global and regional scales during the 1980-2010 period, Climatic Change, 109, 163–190, https://doi.org/10.1007/s10584-011-0154-1, 2011.

Grimsdell, A. W., Alexander, M. J., May, P. T., and Hoffmann, L.: Model Study of Waves Generated by Convection with Direct Validation via Satellite, J. Atmos. Sci., 67, 1617 – 1631, https://doi.org/10.1175/2009JAS3197.1, https://journals.ametsoc.org/view/journals/atsc/67/5/2009jas3197.1.xml, 2010.

Hanson, D. R. and Mauersberger, K.: Laboratory studies of the nitric acid trihydrate: Implications for the south polar stratosphere, Geophys. Res. Lett., 15, 855–858, https://doi.org/10.1029/GL015i008p00855, 1988.

Hervig, M. E. and Deshler, T.: Stratospheric aerosol surface area and volume inferred from HALOE, CLAES, and ILAS measurements, J. Geophys. Res.: Atmos., 103, 25 345–25 352, https://doi.org/10.1029/98JD01962, 1998.

Hoffmann, L. and Alexander, M. J.: Occurrence frequency of convective gravity waves during the North American thunderstorm season, J. Geophys. Res.: Atmos., 115, https://doi.org/10.1029/2010JD014401, 2010.

Hoffmann, L., Xue, X., and Alexander, M. J.: A global view of stratospheric gravity wave hotspots located with Atmospheric Infrared Sounder observations, Journal of Geophysical Research: Atmospheres, 118, 416–434, https://doi.org/10.1029/2012JD018658, 2013.

Hoffmann, L., Alexander, M. J., Clerbaux, C., Grimsdell, A. W., Meyer, C. I., Rößler, T., and Tournier, B.: Intercomparison of stratospheric gravity wave observations with AIRS and IASI, Atmospheric Measurement Techniques, 7, 4517–4537, https://doi.org/10.5194/amt-7-4517-2014, https://www.atmos-meas-tech.net/7/4517/2014/, 2014.

Hoffmann, L., Grimsdell, A. W., and Alexander, M. J.: Stratospheric gravity waves at Southern Hemisphere orographic hotspots: 2003–2014 AIRS/Aqua observations, Atmos. Chem. Phys., 16, 9381–9397, https://doi.org/10.5194/acp-16-9381-2016, 2016.

Hoffmann, L., Spang, R., Orr, A., Alexander, M. J., Holt, L. A., and Stein, O.: A decadal satellite record of gravity wave activity in the lower stratosphere to study polar stratospheric cloud formation, Atmos. Chem. Phys., 17, 2901–2920, https://doi.org/10.5194/acp-17-2901-2017, 2017.

Höpfner, M., Larsen, N., Spang, R., Luo, B. P., Ma, J., Svendsen, S. H., Eckermann, S. D., Knudsen, B., Massoli, P., Cairo, F., Stiller, G., v. Clarmann, T., and Fischer, H.: MIPAS detects Antarctic stratospheric belt of NAT PSCs caused by mountain waves, Atmos. Chem. Phys., 6, 1221–1230, https://doi.org/10.5194/acp-6-1221-2006, 2006a.

Höpfner, M., Luo, B. P., Massoli, P., Cairo, F., Spang, R., Snels, M., Di Donfrancesco, G., Stiller, G., von Clarmann, T., Fischer, H., and Biermann, U.: Spectroscopic evidence for NAT, STS, and ice in MIPAS infrared limb emission measurements of polar stratospheric clouds, Atmos. Chem. Phys., 6, 1201–1219, https://doi.org/10.5194/acp-6-1201-2006, 2006b.

Höpfner, M., Pitts, M. C., and Poole, L. R.: Comparison between CALIPSO and MIPAS observations of polar stratospheric clouds, J. Geophys. Res.: Atmos., 114, https://doi.org/10.1029/2009JD012114, d00H05, 2009.

Höpfner, M., Deshler, T., Pitts, M., Poole, L., Spang, R., Stiller, G., and von Clarmann, T.: The MIPAS/Envisat climatology (2002–2012) of polar stratospheric cloud volume density profiles, Atmos. Meas. Tech., 11, 5901–5923, https://doi.org/10.5194/amt-11-5901-2018, 2018.

Hoyle, C. R., Engel, I., Luo, B. P., Pitts, M. C., Poole, L. R., Grooß, J.-U., and Peter, T.: Heterogeneous formation of polar stratospheric clouds – Part 1: Nucleation of nitric acid trihydrate (NAT), Atmos. Chem. Phys., 13, 9577–9595, https://doi.org/10.5194/acp-13-9577-2013, 2013.

1060   Jähn, M., Kuhlmann, G., Mu, Q., Haussaire, J.-M., Ochsner, D., Osterried, K., Clément, V., and Brunner, D.: An online emission module for atmospheric chemistry transport models: implementation in COSMO-GHG v5.6a and COSMO-ART v5.1-3.1, Geosci. Model Dev., 13, 2379–2392, https://doi.org/10.5194/gmd-13-2379-2020, https://gmd.copernicus.org/articles/13/2379/2020/, 2020.

Janssens-Maenhout, G., Petrescu, A. M., Muntean, M., and Blujdea, V.: Verifying Greenhouse Gas Emissions: Methods to Support International Climate Agreements, Greenhouse Gas Measurement and Management, 1, 132–133, https://doi.org/10.1080/20430779.2011.579358, 1065   2011.

Janssens-Maenhout, G., Diego, V., and Marilena Muntean, G.: Global emission inventories in the Emission Database for Global Atmospheric Research (EDGAR)–Manual (I), Gridding: EDGAR emissions distribution on global gridmaps, Publications Office of the European Union, Luxembourg, 2013.

Jöckel, P., Kerkweg, A., Pozzer, A., Sander, R., Tost, H., Riede, H., Baumgaertner, A., Gromov, S., and Kern, B.: Development cycle 2 of the 1070   Modular Earth Submodel System (MESSy2), Geosci. Model Dev., 3, 717–752, https://doi.org/10.5194/gmd-3-717-2010, 2010.

Jöckel, P., Tost, H., Pozzer, A., Kunze, M., Kirner, O., Brenninkmeijer, C. A. M., Brinkop, S., Cai, D. S., Dyroff, C., Eckstein, J., Frank, F., Garny, H., Gottschaldt, K.-D., Graf, P., Grewe, V., Kerkweg, A., Kern, B., Matthes, S., Mertens, M., Meul, S., Neumaier, M., Nützel, M., Oberländer-Hayn, S., Ruhnke, R., Runde, T., Sander, R., Scharffe, D., and Zahn, A.: Earth System Chemistry integrated Modelling (ES-CiMo) with the Modular Earth Submodel System (MESSy) version 2.51, Geosci. Model Dev., 9, 1153–1200, https://doi.org/10.5194/gmd-1075   9-1153-2016, 2016.

Junge, C. E., Chagnon, C. W., and Manson, J. E.: Stratospheric Aerosols, J. Meteor., 18, 81–108, https://doi.org/10.1175/1520-0469(1961)018<0081:SA>2.0.CO;2, 1961.

Kang, M.-J., Chun, H.-Y., and Kim, Y.-H.: Momentum Flux of Convective Gravity Waves Derived from an Offline Gravity Wave Parameterization. Part I: Spatiotemporal Variations at Source Level, J. Atmos. Sci., 74, 3167 – 3189, https://doi.org/10.1175/JAS-D-17-0053.1, 1080   https://journals.ametsoc.org/view/journals/atsc/74/10/jas-d-17-0053.1.xml, 2017.

Kelly, K. K., Tuck, A. F., Murphy, D. M., Proffitt, M. H., Fahey, D. W., Jones, R. L., McKenna, D. S., Loewenstein, M., Podolske, J. R., Strahan, S. E., Ferry, G. V., Chan, K. R., Vedder, J. F., Gregory, G. L., Hypes, W. D., McCormick, M. P., Browell, E. V., and Heidt, L. E.: Dehydration in the lower Antarctic stratosphere during late winter and early spring, 1987, J. Geophys. Res.: Atmos., 94, 11 317–11 357, https://doi.org/10.1029/JD094iD09p11317, 1989.

1085   Kennard, E. H.: Kinetic theory of gases, with an introduction to statistical mechanics, McGraw-Hill Book Company, New York and London, https://archive.org/details/in.ernet.dli.2015.1789, 1938.

Khaykin, S. M., Engel, I., Vömel, H., Formanyuk, I. M., Kivi, R., Korshunov, L. I., Krämer, M., Lykov, A. D., Meier, S., Naebert, T., Pitts, M. C., Santee, M. L., Spelten, N., Wienhold, F. G., Yushkov, V. A., and Peter, T.: Arctic stratospheric dehydration – Part 1: Unprecedented observation of vertical redistribution of water, Atmos. Chem. Phys., 13, 11 503–11 517, https://doi.org/10.5194/acp-13-11503-2013, 2013.

1090   Khosrawi, F., Kirner, O., Stiller, G., Höpfner, M., Santee, M. L., Kellmann, S., and Braesicke, P.: Comparison of ECHAM5/MESSy Atmospheric Chemistry (EMAC) simulations of the Arctic winter 2009/2010 and 2010/2011 with Envisat/MIPAS and Aura/MLS observations, Atmos. Chem. Phys., 18, 8873–8892, https://doi.org/10.5194/acp-18-8873-2018, 2018.

Kirner, O., Ruhnke, R., Buchholz-Dietsch, J., Jöckel, P., Bruehl, C., and Steil, B.: Simulation of polar stratospheric clouds in the chemistry-climate-model EMAC via the submodel PSC, Geosci. Model Dev., 4, 169–182, https://doi.org/10.5194/gmd-4-169-2011, 2011.

1095   Kirner, O., Müller, R., Ruhnke, R., and Fischer, H.: Contribution of liquid, NAT and ice particles to chlorine activation and ozone depletion in Antarctic winter and spring, Atmos. Chem. Phys., 15, 2019–2030, https://doi.org/10.5194/acp-15-2019-2015, 2015.

Koop, T., Luo, B., Tsias, A., and Peter, T.: Water activity as the determinant for homogeneous ice nucleation in aqueous solutions, Nature, 406, https://doi.org/10.1038/35020537, 2000.

Krieger, U. K., Mössinger, J. C., Luo, B., Weers, U., and Peter, T.: Measurement of the refractive indices of H2SO4–HNO3–H2O so-
1100   lutions to stratospheric temperatures, Appl. Opt., 39, 3691–3703, https://doi.org/10.1364/AO.39.003691, http://ao.osa.org/abstract.cfm? URI=ao-39-21-3691, 2000.

Lamarque, J.-F., Bond, T. C., Eyring, V., Granier, C., Heil, A., Klimont, Z., Lee, D., Liousse, C., Mieville, A., Owen, B., Schultz, M. G., Shindell, D., Smith, S. J., Stehfest, E., Van Aardenne, J., Cooper, O. R., Kainuma, M., Mahowald, N., McConnell, J. R., Naik, V., Riahi, K., and van Vuuren, D. P.: Historical (1850-2000) gridded anthropogenic and biomass burning emissions of reactive gases and aerosols:
1105   methodology and application, Atmos. Chem. Phys., 10, 7017–7039, https://doi.org/10.5194/acp-10-7017-2010, 2010.

Lamarque, J.-F., Shindell, D. T., Josse, B., Young, P. J., Cionni, I., Eyring, V., Bergmann, D., Cameron-Smith, P., Collins, W. J., Doherty, R., Dalsoren, S., Faluvegi, G., Folberth, G., Ghan, S. J., Horowitz, L. W., Lee, Y. H., MacKenzie, I. A., Nagashima, T., Naik, V., Plummer, D., Righi, M., Rumbold, S. T., Schulz, M., Skeie, R. B., Stevenson, D. S., Strode, S., Sudo, K., Szopa, S., Voulgarakis, A., and Zeng, G.: The Atmospheric Chemistry and Climate Model Intercomparison Project (ACCMIP): overview and description of models, simulations
1110   and climate diagnostics, Geosci. Model Dev., 6, 179–206, https://doi.org/10.5194/gmd-6-179-2013, https://gmd.copernicus.org/articles/6/ 179/2013/, 2013.

Langematz, U., M. Tully (Lead Authors), Calvo, N., Dameris, M., de Laat, A. T. J., Klekociuk, A., Müller, R., and Young, P.: Chapter 4: Polar Stratospheric Ozone: Past, Present, and Future, in: Scientific Assessment of Ozone Depletion: 2018, edited by Fahey, D. W., Newman, P. A., Pyle, J. A., and Safari, B., Global Ozone Research and Monitoring Project – Report No. 58, World Meteorological Organization,
1115   Geneva, Switzerland, 2018.

Leuenberger, D., Koller, M., Fuhrer, O., and Schär, C.: A Generalization of the SLEVE Vertical Coordinate, Mon. Weather Rev., 138, 3683–3689, https://doi.org/10.1175/2010MWR3307.1, 2010.

Lickley, M., Solomon, S., Fletcher, S., Velders, G. J. M., Daniel, J., Rigby, M., Montzka, S. A., Kuijpers, L. J. M., and Stone, K.: Quan-
tifying contributions of chlorofluorocarbon banks to emissions and impacts on the ozone layer and climate, Nature Comm., 11, 1380,
1120   https://doi.org/10.1038/s41467-020-15162-7, 2020.

Mann, G. W., Carslaw, K. S., Chipperfield, M. P., Davies, S., and Eckermann, S. D.: Large nitric acid trihydrate particles and denitrification caused by mountain waves in the Arctic stratosphere, J. Geophys. Res.: Atmos., 110, https://doi.org/10.1029/2004JD005271, d08202, 2005.

Marti, J. and Mauersberger, K.: A survey and new measurements of ice vapor pressure at temperatures between 170 and 250K, Geophys.
1125   Res. Lett., 20, 363–366, https://doi.org/10.1029/93GL00105, 1993.

McDonald, A. J., George, S. E., and Woollands, R. M.: Can gravity waves significantly impact PSC occurrence in the Antarctic?, Atmos. Chem. Phys., 9, 8825–8840, https://doi.org/10.5194/acp-9-8825-2009, 2009.

Meilinger, S. K., Koop, T., Luo, B. P., Huthwelker, T., Carslaw, K. S., Krieger, U., Crutzen, P. J., and Peter, T.: Size-dependent stratospheric droplet composition in Lee wave temperature fluctuations and their potential role in PSC freezing, Geophys. Res. Lett., 22, 3031–3034,
1130   https://doi.org/10.1029/95GL03056, 1995.

Middlebrook, A. M., Berland, B. S., George, S. M., Tolbert, M. A., and Toon, O. B.: Real refractive indices of infrared-characterized nitric-acid/ice films: Implications for optical measurements of polar stratospheric clouds, J. Geophys. Res.: Atmospheres, 99, 25 655–25 666, https://doi.org/https://doi.org/10.1029/94JD02391, https://agupubs.onlinelibrary.wiley.com/doi/abs/10.1029/94JD02391, 1994.

Mishchenko, M. I., Travis, L. D., and Mackowski, D. W.: T-matrix computations of light scattering by nonspherical particles: A review, J. Quant. Spectrosc. Radiat. Transf., 55, 535 – 575, https://doi.org/https://doi.org/10.1016/0022-4073(96)00002-7, http://www.sciencedirect.com/science/article/pii/0022407396000027, light Scattering by Non-Spherical Particles, 1996.

Montzka, S. A., Dutton, G. S., Yu, P., Ray, E., Portmann, R. W., Daniel, J. S., Kuijpers, L., Hall, B. D., Mondeel, D., Siso, C., Nance, J. D., Rigby, M., Manning, A. J., Hu, L., Moore, F., Miller, B. R., and Elkins, J. W.: An unexpected and persistent increase in global emissions of ozone-depleting CFC-11, Nature, 557, 413–417, https://doi.org/10.1038/s41586-018-0106-2, 2018.

Morgenstern, O., Giorgetta, M., and Shibata, K.: Chemsitry Climate Models and Scenarios, in: SPARC CCMVal Report on the Evaluation of Chemistry-Climate Models, edited by Eyring, V., Shepherd, T., and Waugh, D., vol. No. 5, p. 426 pp., SPARC Office, http://www.sparc-climate.org/publications/sparc-reports/, 2010.

Morgenstern, O., Hegglin, M. I., Rozanov, E., O'Connor, F. M., Abraham, N. L., Akiyoshi, H., Archibald, A. T., Bekki, S., Butchart, N., Chipperfield, M. P., Deushi, M., Dhomse, S. S., Garcia, R. R., Hardiman, S. C., Horowitz, L. W., Jöckel, P., Josse, B., Kinnison, D., Lin, M., Mancini, E., Manyin, M. E., Marchand, M., Marécal, V., Michou, M., Oman, L. D., Pitari, G., Plummer, D. A., Revell, L. E., Saint-Martin, D., Schofield, R., Stenke, A., Stone, K., Sudo, K., Tanaka, T. Y., Tilmes, S., Yamashita, Y., Yoshida, K., and Zeng, G.: Review of the global models used within phase 1 of the Chemistry–Climate Model Initiative (CCMI), Geoscientific Model Development, 10, 639–671, https://doi.org/10.5194/gmd-10-639-2017, https://gmd.copernicus.org/articles/10/639/2017/, 2017.

Murphy, D. M. and Ravishankara, A. R.: Temperature averages and rates of stratospheric reactions, Geophysical Research Letters, 21, 2471–2474, https://doi.org/https://doi.org/10.1029/94GL02287, https://agupubs.onlinelibrary.wiley.com/doi/abs/10.1029/94GL02287, 1994.

Nakajima, H., Murata, I., Nagahama, Y., Akiyoshi, H., Saeki, K., Kinase, T., Takeda, M., Tomikawa, Y., Dupuy, E., and Jones, N. B.: Chlorine partitioning near the polar vortex edge observed with ground-based FTIR and satellites at Syowa Station, Antarctica, in 2007 and 2011, Atmos. Chem. Phys., 20, 1043–1074, https://doi.org/10.5194/acp-20-1043-2020, 2020.

Nash, E. R., Newman, P. A., Rosenfield, J. E., and Schoeberl, M. R.: An objective determination of the polar vortex using Ertel's potential vorticity, J. Geophys. Res.: Atmos., 101, 9471–9478, https://doi.org/10.1029/96JD00066, 1996.

Noel, V. and Pitts, M.: Gravity wave events from mesoscale simulations, compared to polar stratospheric clouds observed from spaceborne lidar over the Antarctic Peninsula, J. Geophys. Res.: Atmos., 117, https://doi.org/10.1029/2011JD017318, 2012.

Noel, V., Hertzog, A., and Chepfer, H.: CALIPSO observations of wave-induced PSCs with near-unity optical depth over Antarctica in 2006–2007, Journal of Geophysical Research: Atmospheres, 114, https://doi.org/https://doi.org/10.1029/2008JD010604, https://agupubs.onlinelibrary.wiley.com/doi/abs/10.1029/2008JD010604, 2009.

Orr, A., Hosking, J. S., Hoffmann, L., Keeble, J., Dean, S. M., Roscoe, H. K., Abraham, N. L., Vosper, S., and Braesicke, P.: Inclusion of mountain-wave-induced cooling for the formation of PSCs over the Antarctic Peninsula in a chemistry–climate model, Atmos. Chem. Phys., 15, 1071–1086, https://doi.org/10.5194/acp-15-1071-2015, 2015.

Orr, A., Hosking, J. S., Delon, A., Hoffmann, L., Spang, R., Moffat-Griffin, T., Keeble, J., Abraham, N. L., and Braesicke, P.: Polar stratospheric clouds initiated by mountain waves in a global chemistry–climate model: a missing piece in fully modelling polar stratospheric ozone depletion, Atmos. Chem. Phys., 20, 12 483–12 497, https://doi.org/10.5194/acp-20-12483-2020, https://acp.copernicus.org/articles/20/12483/2020/, 2020.

Peter, T.: Microphysics and heterogeneous chemistry of polar stratospheric clouds, Annu. Rev. Phys. Chem., 48, 785–822, https://doi.org/10.1146/annurev.physchem.48.1.785, pMID: 15012456, 1997.

1170 Peter, T. and Grooß, J.-U.: Chapter 4 Polar Stratospheric Clouds and Sulfate Aerosol Particles: Microphysics, Denitrification and Hetero-geneous Chemistry, in: Stratospheric Ozone Depletion and Climate Change, edited by Müller, R., pp. 108–144, The Royal Society of Chemistry, https://doi.org/10.1039/9781849733182-00108, http://dx.doi.org/10.1039/9781849733182-00108, 2012.

Pitts, M. C., Poole, L. R., and Thomason, L. W.: CALIPSO polar stratospheric cloud observations: second-generation detection algorithm and composition discrimination, Atmos. Chem. Phys., 9, 7577–7589, https://doi.org/10.5194/acp-9-7577-2009, 2009.

1175 Pitts, M. C., Poole, L. R., and Gonzalez, R.: Polar stratospheric cloud climatology based on CALIPSO spaceborne lidar measurements from 2006 to 2017, Atmos. Chem. Phys., 18, 10 881–10 913, https://doi.org/10.5194/acp-18-10881-2018, 2018.

Plougonven, R., Hertzog, A., and Teitelbaum, H.: Observations and simulations of a large-amplitude mountain wave breaking over the Antarctic Peninsula, J. Geophys. Res.: Atmospheres, 113, https://doi.org/10.1029/2007JD009739, 2008.

Prather, M. J.: Photolysis rates in correlated overlapping cloud fields: Cloud-J 7.3c, Geosci. Model Dev., 8, 2587–2595, 1180 https://doi.org/10.5194/gmd-8-2587-2015, 2015.

Preusse, P., Ern, M., Bechtold, P., Eckermann, S. D., Kalisch, S., Trinh, Q. T., and Riese, M.: Characteristics of gravity waves resolved by ECMWF, Atmospheric Chemistry and Physics, 14, 10 483–10 508, https://doi.org/10.5194/acp-14-10483-2014, https://acp.copernicus.org/articles/14/10483/2014/, 2014.

Queney, P.: Theory of perturbations in stratified currents with applications to air flow over mountain barriers, University of Chicago Press, 1185 Chicago, Ill, 1947.

Reinert, D., Prill, F., Zängl, G., Rieger, D., Schröter, J., Förstner, J., Werchner, S., Weimer, M., Ruhnke, R., and Vogel, B.: Working with the ICON Model, Tech. rep., Deutscher Wetterdienst, Offenbach, https://code.mpimet.mpg.de/attachments/download/19568/ICON_tutorial_2019.pdf, 2019.

Rieger, D., Bangert, M., Bischoff-Gauss, I., Förstner, J., Lundgren, K., Reinert, D., Schröter, J., Vogel, H., Zängl, G., Ruhnke, R., and 1190 Vogel, B.: ICON-ART 1.0 - a new online-coupled model system from the global to regional scale, Geosci. Model Dev., 8, 1659–1676, https://doi.org/10.5194/gmd-8-1659-2015, 2015.

Salcedo, D., Molina, L. T., and Molina, M. J.: Homogeneous Freezing of Concentrated Aqueous Nitric Acid Solutions at Polar Stratospheric Temperatures, J. Phys. Chem., 105, 1433–1439, https://doi.org/10.1021/jp001639s, 2001.

Sander, R., Baumgaertner, A., Gromov, S., Harder, H., Jöckel, P., Kerkweg, A., Kubistin, D., Regelin, E., Riede, H., Sandu, A., Tarabor-1195 relli, D., Tost, H., and Xie, Z.-Q.: The atmospheric chemistry box model CAABA/MECCA-3.0, Geosci. Model Dev., 4, 373–380, https://doi.org/10.5194/gmd-4-373-2011, 2011a.

Sander, S., Abbatt, J., Barker, J., Burkholder, J., Friedl, R., Golden, D., Huie, R., Kolb, C., Kurylo, M., Moortgat, K., Orkin, V., and Wine, P.: Chemical Kinetics and Photochemical Data for Use in Atmospheric Studies, Evaluation No. 17, JPL Publication 10-6, 2011b.

Sandu, A. and Sander, R.: Technical note: Simulating chemical systems in Fortran90 and Matlab with the Kinetic PreProcessor KPP-2.1, 1200 Atmos. Chem. Phys., 6, 187–195, https://doi.org/10.5194/acp-6-187-2006, 2006.

Schoeberl, M. and Newman, P.: MIDDLE ATMOSPHERE, Polar Vortex, in: Encyclopedia of Atmospheric Sciences, edited by Holton, J. R., pp. 1321–1328, Academic Press, Oxford, https://doi.org/https://doi.org/10.1016/B0-12-227090-8/00228-1, 2003.

Schröter, J., Rieger, D., Stassen, C., Vogel, H., Weimer, M., Werchner, S., Förstner, J., Prill, F., Reinert, D., Zängl, G., Giorgetta, M., Ruhnke, R., Vogel, B., and Braesicke, P.: ICON-ART 2.1: a flexible tracer framework and its application for composition studies in numerical 1205 weather forecasting and climate simulations, Geosci. Model Dev., 11, 4043–4068, https://doi.org/10.5194/gmd-11-4043-2018, 2018.

Sedona, R., Hoffmann, L., Spang, R., Cavallaro, G., Griessbach, S., Höpfner, M., Book, M., and Riedel, M.: Exploration of machine learning methods for the classification of infrared limb spectra of polar stratospheric clouds, Atmos. Meas. Tech., 13, 3661–3682, https://doi.org/10.5194/amt-13-3661-2020, https://amt.copernicus.org/articles/13/3661/2020/, 2020.

Seinfeld, J. H. and Pandis, S. N.: Atmospheric Chemistry and Physics: From Air Pollution to Climate Change, Wiley, Hoboken, NJ, 2. ed. edn., previous ed.: 1998, 2006.

Sindelarova, K., Granier, C., Bouarar, I., Guenther, A., Tilmes, S., Stavrakou, T., Müller, J.-F., Kuhn, U., Stefani, P., and Knorr, W.: Global data set of biogenic VOC emissions calculated by the MEGAN model over the last 30 years, Atmos. Chem. Phys., 14, 9317–9341, https://doi.org/10.5194/acp-14-9317-2014, 2014.

Solomon, S.: Stratospheric ozone depletion: A review of concepts and history, Rev. Geophys., 37, 275–316, https://doi.org/10.1029/1999RG900008, 1999.

Solomon, S., Garcia, R., Rowland, F., and Wuebbles: On the depletion of Antarctic ozone, Nature, 321, 755–758, https://doi.org/10.1038/321755a0, 1986.

Solomon, S., Kinnison, D., Bandoro, J., and Garcia, R.: Simulation of polar ozone depletion: An update, J. Geophys. Res.: Atmos., 120, 7958–7974, https://doi.org/10.1002/2015JD023365, 2015.

Spang, R., Hoffmann, L., Höpfner, M., Griessbach, S., Müller, R., Pitts, M. C., Orr, A. M. W., and Riese, M.: A multi-wavelength classification method for polar stratospheric cloud types using infrared limb spectra, Atmos. Meas. Tech., 9, 3619–3639, https://doi.org/10.5194/amt-9-3619-2016, 2016.

Spang, R., Hoffmann, L., Müller, R., Grooß, J.-U., Tritscher, I., Höpfner, M., Pitts, M., Orr, A., and Riese, M.: A climatology of polar stratospheric cloud composition between 2002 and 2012 based on MIPAS/Envisat observations, Atmos. Chem. Phys., 18, 5089–5113, https://doi.org/10.5194/acp-18-5089-2018, 2018.

SPARC: SPARC Newsletter No. 40, available at http://www.sparc-climate.org/publications/newsletter, 2013.

Staniforth, A. and Thuburn, J.: Horizontal grids for global weather and climate prediction models: a review, Q. J. Roy. Meteor. Soc., 138, 1–26, https://doi.org/10.1002/qj.958, 2012.

Steiner, M., Luo, B., Peter, T., Pitts, M. C., and Stenke, A.: Evaluation of polar stratospheric clouds in the global chemistry–climate model SOCOLv3.1 by comparison with CALIPSO spaceborne lidar measurements, Geosci. Model Dev., 14, 935–959, https://doi.org/10.5194/gmd-14-935-2021, https://gmd.copernicus.org/articles/14/935/2021/, 2021.

Stephens, G. L., Vane, D. G., Boain, R. J., Mace, G. G., Sassen, K., Wang, Z., Illingworth, A. J., O'connor, E. J., Rossow, W. B., Durden, S. L., Miller, S. D., Austin, R. T., Benedetti, A., and Mitrescu, C. a.: The CloudSat Mission and the A-Train, B. Am. Meteorol. Soc., 83, 1771–1790, https://doi.org/10.1175/BAMS-83-12-1771, 2002.

Stokes, G. G.: On the Effect of the Internal Friction of Fluids on the Motion of Pendulums, Transactions of the Cambridge Philosophical Society, Part II, 8 – 106, 1851.

Stone, K. A., Solomon, S., Kinnison, D. E., Baggett, C. F., and Barnes, E. A.: Prediction of Northern Hemisphere Regional Surface Temperatures Using Stratospheric Ozone Information, J. Geophys. Res.: Atmos., 124, 5922–5933, https://doi.org/10.1029/2018JD029626, 2019.

Svendsen, S. H., Larsen, N., Knudsen, B., Eckermann, S. D., and Browell, E. V.: Influence of mountain waves and NAT nucleation mechanisms on polar stratospheric cloud formation at local and synoptic scales during the 1999-2000 Arctic winter, Atmos. Chem. Phys., 5, 739–753, https://doi.org/10.5194/acp-5-739-2005, 2005.

Tabazadeh, A., Santee, M. L., Danilin, M. Y., Pumphrey, H. C., Newman, P. A., Hamill, P. J., and Mergenthaler, J. L.: Quantifying Denitrification and Its Effect on Ozone Recovery, Science, 288, 1407–1411, https://doi.org/10.1126/science.288.5470.1407, 2000.

Taylor, K., Williamson, D., and Zwiers, F.: The Sea Surface Temperature and Sea-ice Concentration Boundary Conditions for AMIP II Simulations, PCMDI report, Program for Climate Model Diagnosis and Intercomparison, Lawrence Livermore National Laboratory, 2000.

Thomason, L. W., Burton, S. P., Luo, B.-P., and Peter, T.: SAGE II measurements of stratospheric aerosol properties at non-volcanic levels, Atmos. Chem. Phys., 8, 983–995, https://doi.org/10.5194/acp-8-983-2008, 2008.

Tritscher, I., Grooß, J.-U., Spang, R., Pitts, M. C., Poole, L. R., Müller, R., and Riese, M.: Lagrangian simulation of ice particles and resulting dehydration in the polar winter stratosphere, Atmos. Chem. Phys., 19, 543–563, https://doi.org/10.5194/acp-19-543-2019, https://acp.copernicus.org/articles/19/543/2019/, 2019.

Tritscher, I., Pitts, M. C., Poole, L. R., Alexander, S. P., Cairo, F., Chipperfield, M. P., Grooß, J.-U., Höpfner, M., Lambert, A., Luo, B. P., Molleker, S., Orr, A., Salawitch, R., Snels, M., Spang, R., Woiwode, W., and Peter, T.: Polar Stratospheric Clouds Satellite Observations, Processes, and Role in Ozone Depletion, Rev. Geophys., n/a, e2020RG000 702, https://doi.org/https://doi.org/10.1029/2020RG000702, https://agupubs.onlinelibrary.wiley.com/doi/abs/10.1029/2020RG000702, e2020RG000702 2020RG000702, 2021.

Tully, M., Klekociuk, A., Alexander, S., Dargaville, R., Deschamps, L., Fraser, P., Gies, H., Henderson, S., Javorniczky, J., Krummel, P., Petelina, S., Shanklin, J., Siddaway, J., and Stone, K.: The Antarctic ozone hole during 2008 and 2009, J. So. Hemisph. Earth, 61, 77–90, https://doi.org/10.22499/2.6101.007, 2011.

van den Broek, M. M. P., Williams, J. E., and Bregman, A.: Implementing growth and sedimentation of NAT particles in a global Eulerian model, Atmos. Chem. Phys., 4, 1869–1883, https://doi.org/10.5194/acp-4-1869-2004, 2004.

van der Werf, G. R., Randerson, J. T., Giglio, L., Collatz, G. J., Kasibhatla, P. S., and Arellano Jr., A. F.: Interannual variability in global biomass burning emissions from 1997 to 2004, Atmos. Chem. Phys., 6, 3423–3441, https://doi.org/10.5194/acp-6-3423-2006, 2006.

van der Werf, G. R., Randerson, J. T., Giglio, L., Collatz, G. J., Mu, M., Kasibhatla, P. S., Morton, D. C., DeFries, R. S., Jin, Y., and van Leeuwen, T. T.: Global fire emissions and the contribution of deforestation, savanna, forest, agricultural, and peat fires (1997-2009), Atmos. Chem. Phys., 10, 11 707–11 735, https://doi.org/10.5194/acp-10-11707-2010, 2010.

Voigt, C., Dörnbrack, A., Wirth, M., Groß, S. M., Pitts, M. C., Poole, L. R., Baumann, R., Ehard, B., Sinnhuber, B.-M., Woiwode, W., and Oelhaf, H.: Widespread polar stratospheric ice clouds in the 2015–2016 Arctic winter – implications for ice nucleation, Atmos. Chem. Phys., 18, 15 623–15 641, https://doi.org/10.5194/acp-18-15623-2018, 2018.

Waibel, A. E., Peter, T., Carslaw, K. S., Oelhaf, H., Wetzel, G., Crutzen, P. J., Pöschl, U., Tsias, A., Reimer, E., and Fischer, H.: Arctic Ozone Loss Due to Denitrification, Science, 283, 2064–2069, https://doi.org/10.1126/science.283.5410.2064, 1999.

Wegner, T., Kinnison, D. E., Garcia, R. R., and Solomon, S.: Simulation of polar stratospheric clouds in the specified dynamics version of the whole atmosphere community climate model, J. Geophys. Res.: Atmospheres, 118, 4991–5002, https://doi.org/https://doi.org/10.1002/jgrd.50415, 2013.

Weimer, M.: Towards Seamless Simulations of Polar Stratospheric Clouds and Ozone in the Polar Stratosphere with ICON-ART, Ph.D. thesis, Karlsruher Institut für Technologie (KIT), https://doi.org/10.5445/IR/1000100338, 2019.

Weimer, M., Mieruch, S., Schädler, G., and Kottmeier, C.: A new estimator of heat periods for decadal climate predictions – a complex network approach, Nonlin. Processes Geophys., 23, 307–317, https://doi.org/10.5194/npg-23-307-2016, 2016.

Weimer, M., Schröter, J., Eckstein, J., Deetz, K., Neumaier, M., Fischbeck, G., Hu, L., Millet, D. B., Rieger, D., Vogel, H., Vogel, B., Reddmann, T., Kirner, O., Ruhnke, R., and Braesicke, P.: An emission module for ICON-ART 2.0: implementation and simulations of acetone, Geosci. Model Dev., 10, 2471–2494, https://doi.org/10.5194/gmd-10-2471-2017, 2017.

Wilka, C., Shah, K., Stone, K., Solomon, S., Kinnison, D., Mills, M., Schmidt, A., and Neely III, R. R.: On the Role of Heterogeneous Chemistry in Ozone Depletion and Recovery, Geophys. Res. Lett., 45, 7835–7842, https://doi.org/10.1029/2018GL078596, 2018.

Winker, D. M., Hunt, W. H., and McGill, M. J.: Initial performance assessment of CALIOP, Geophys. Res. Lett., 34, https://doi.org/10.1029/2007GL030135, 2007.

Wright, C. J., Hindley, N. P., Hoffmann, L., Alexander, M. J., and Mitchell, N. J.: Exploring gravity wave characteristics in 3-D using a novel S-transform technique: AIRS/Aqua measurements over the Southern Andes and Drake Passage, Atmos. Chem. Phys., 17, 8553–8575, https://doi.org/10.5194/acp-17-8553-2017, 2017.

Zambri, B., Solomon, S., Kinnison, D. E., Mills, M. J., Schmidt, A., Neely III, R. R., Bourassa, A. E., Degenstein, D. A., and Roth, C. Z.: Modeled and Observed Volcanic Aerosol Control on Stratospheric NOy and Cly, J. Geophys. Res.: Atmos., 124, 10 283–10 303, https://doi.org/10.1029/2019JD031111, 2019.

Zängl, G., Reinert, D., Rípodas, P., and Baldauf, M.: The ICON (ICOsahedral Non-hydrostatic) modelling framework of DWD and MPI-M: Description of the non-hydrostatic dynamical core, Q. J. R. Meteorol. Soc., 141, 563–579, https://doi.org/10.1002/qj.2378, 2015.

Zhu, Y., Toon, O. B., Lambert, A., Kinnison, D. E., Brakebusch, M., Bardeen, C. G., Mills, M. J., and English, J. M.: Development of a Polar Stratospheric Cloud Model within the Community Earth System Model using constraints on Type I PSCs from the 2010-2011 Arctic winter, J. Adv. Model. Earth Sy., 7, 551–585, https://doi.org/10.1002/2015MS000427, 2015.

Zhu, Y., Toon, O. B., Pitts, M. C., Lambert, A., Bardeen, C., and Kinnison, D. E.: Comparing simulated PSC optical properties with CALIPSO observations during the 2010 Antarctic winter, J. Geophys. Res.: Atmos., 122, 1175–1202, https://doi.org/10.1002/2016JD025191, 2017.